The Astrophysical Journal, 990:211 (22pp), 2025 September 10 https://doi.org/10.3847/1538-4357/ad9f3d

Gravitational-wave Phase Shifts in Eccentric Black Hole Mergers as a Probe of Dynamical Formation Environments

Johan Samsing[1,2], Kai Hendriks[1,2], Lorenz Zwick[1,2], Daniel J. D'Orazio[1], and Bin Liu[1,3]
[1] Niels Bohr International Academy, The Niels Bohr Institute, Blegdamsvej 17, DK-2100, Copenhagen, Denmark; jsamsing@gmail.com
[2] Center of Gravity, Niels Bohr Institute, Blegdamsvej 17, 2100 Copenhagen, Denmark
[3] Institute for Astronomy, School of Physics, Zhejiang University, 310058 Hangzhou, People's Republic of China

Received 2024 April 16; revised 2024 December 10; accepted 2024 December 12; published 2025 September 9

Abstract

We here quantify the gravitational-wave (GW) phase shift appearing in the waveform of eccentric binary black hole (BBH) mergers formed dynamically in 3-body systems. For this, we have developed a novel numerical method where we construct a reference binary, by evolving the post-Newtonian ($\mathcal{PN}$) evolution equations backwards from a point near merger without the inclusion of the third object, that can be compared to the perturbed binary that evolves under the influence from the third BH. From this, we quantify how the interplay between dynamical tides, $\mathcal{PN}$-effects, and the time-dependent Doppler shift of the eccentric GW source results in unique observable GW phase shifts that can be used to probe the dynamical assembly mechanism of individual GW sources. We further find an analytical expression for the GW phase shift, which has a universal functional form that only depends on the time-evolving BBH eccentricity. The normalization scales with the BH masses and initial separation, which can be linked to the underlying astrophysical environment. GW phase shifts from a chaotic 3-body BH scattering taking place in a cluster, and from a BBH inspiraling in a disk migration trap near a supermassive BH, are also shown for illustration.

Unified Astronomy Thesaurus concepts: Astrophysical black holes (98); Gravitational wave astronomy (675); Gravitational wave sources (677); Gravitational waves (678); Astrodynamics (76); N-body simulations (1083); Stellar mass black holes (1611); Black holes (162)

1. Introduction

The number of merging binary black holes (BBHs) observed in gravitational waves (GWs) with LIGO/Virgo/Kagra (LVK) is steadily increasing (R. Abbott et al. 2023). However, how these mergers form in our Universe is still a major unsolved question, and with a possibly wide variety of observed black hole (BH) spins (B. Zackay et al. 2019; J. Garcìa-Bellido et al. 2021), masses (B. P. Abbott et al. 2019a; R. Abbott et al. 2020), and possibly eccentricity (B. P. Abbott et al. 2019b; I. Romero-Shaw et al. 2021; V. Gayathri et al. 2022; I. Romero-Shaw et al. 2022; N. Gupte et al. 2024: The LIGO Scientific Collaboration et al. 2024), nature likely assemble these BBHs in a variety of different ways. Some proposed formation environments include dense stellar clusters (S. F. Portegies Zwart & S. L. W. McMillan 2000; S. Banerjee et al. 2010; W. H. Lee et al. 2010; A. Tanikawa 2013; Y.-B. Bae et al. 2014; E. Ramirez-Ruiz et al. 2015; C. L. Rodriguez et al. 2015, 2016a, 2016b; A. Askar et al. 2017; D. Park et al. 2017; J. Samsing 2018; J. Samsing & D. J. D'Orazio 2018; J. Samsing et al. 2020; A. A. Trani et al. 2021, 2022), isolated binary stars (M. Dominik et al. 2012, 2013, 2015; K. Belczynski et al. 2016a, 2016b; A. Murguia-Berthier et al. 2017; K. Silsbee & S. Tremaine 2017; C. L. Rodriguez & F. Antonini 2018; S. L. Schroder et al. 2018; G. Iorio et al. 2023), hierarchical systems (S. Naoz et al. 2013; G. Li et al. 2014; J. M. O. Antognini & T. A. Thompson 2016; F. Antonini et al. 2016; K. Silsbee & S. Tremaine 2017; L. Randall & Z.-Z. Xianyu 2018; A. S. Hamers & T. A. Thompson 2019; M. A. S. Martinez et al. 2020; B. Liu & D. Lai 2021; A. A. Trani et al. 2022), active galactic nuclei (AGN) disks (I. Bartos et al. 2017; N. C. Stone et al. 2017; B. McKernan et al. 2018; H. Tagawa et al. 2020; J. Samsing et al. 2022; G. Fabj & J. Samsing 2024; B. Rom et al. 2024; A. A. Trani et al. 2024), galactic nuclei (GN; R. M. O'Leary et al. 2009; J. Hong & H. M. Lee 2015; F. Antonini & F. A. Rasio 2016; A. P. Stephan et al. 2016; J. H. VanLandingham et al. 2016; A. S. Hamers et al. 2018; B.-M. Hoang et al. 2018; B. Liu et al. 2019a; A. A. Trani et al. 2019; B. Liu & D. Lai 2021; D. Atallah et al. 2023), very massive stellar mergers (A. Loeb 2016; S. E. Woosley 2016; A. Janiuk et al. 2017; D. J. D'Orazio & A. Loeb 2018), and single–single GW captures of primordial black holes (S. Bird et al. 2016; B. Carr et al. 2016; I. Cholis et al. 2016; M. Sasaki et al. 2016). But how do we observationally disentangle these channels?

The success of LVK only marks the beginning of this new field, as new proposed observatories, such as the Earth-based 3G-observatories the Einstein Telescope (ET; M. Maggiore et al. 2020) and Cosmic Explorer (CE; M. Evans et al. 2023), and the space-borne DECIGO/TianQin/Taiji (S. Kawamura et al. 2011; J. Luo et al. 2016; W.-R. Hu & Y.-L. Wu 2017; S. Liu et al. 2020; deci-Hertz) and LISA (P. Amaro-Seoane et al. 2017; milli-Hertz) not only will expand our observable window in GW frequency allowing for multiband GW observations (e.g., A. Sesana 2016) but also will be much more sensitive leading to an estimated $\sim 10^5$ observed mergers per year near the current LVK bands. This will not only make it more likely to observe some of the rare and more scientifically valuable GW sources but also make it possible to build up solid statistics in order to gain new insight into the compact-object merger history as a function of redshift (e.g., M. Fishbach et al. 2018; I. M. Romero-Shaw et al. 2021; S. Biscoveanu et al. 2022; L. A. C. van Son et al. 2022; M. Fishbach & G. Fragione 2023), as well as constraining cosmology (e.g., W. M. Farr et al. 2019).

The variety of proposed formation channels is large, and it seems very challenging with current methods to tell individual channels apart using GWs alone (e.g., M. Zevin et al. 2021a). However, certain groups of channels are likely to be distinguishable from each other, e.g., BBHs forming through dynamical interactions will give rise to a significant fraction of eccentric mergers (e.g., K. Gültekin et al. 2006; J. Samsing et al. 2014, 2018, 2018, 2019, 2020; J. Samsing & E. Ramirez-Ruiz 2017; C. L. Rodriguez et al. 2018a; J. Samsing 2018; J. Samsing & T. Ilan 2018; J. Samsing & D. J. D'Orazio 2018; B. Liu et al. 2019b; M. Zevin et al. 2019; M. Zevin et al. 2021b) with distinct distributions in LVK (J. Samsing 2018), DECIGO/TianQin/Taiji (e.g., X. Chen & P. Amaro-Seoane 2017; J. Samsing et al. 2020), and LISA (K. Breivik et al. 2016; D. J. D'Orazio & J. Samsing 2018; J. Samsing & D. J. D'Orazio 2018; K. Kremer et al. 2019), in contrast to those forming through isolated binary evolution. Other parameters include the relative spin orientation of the merging BBHs (e.g., V. Kalogera 2000; C. L. Rodriguez et al. 2016c; B. Liu & D. Lai 2018), as well as the mass spectrum (e.g., M. Zevin et al. 2017; Y. Su et al. 2021). Although this is encouraging, the group of dynamically formed BBH mergers consists likewise of several subchannels that again overlap in their observed quantities. For example, systems in hierarchical Lidov–Kozai–triple configurations (e.g., B.-M. Hoang et al. 2018; B. Liu et al. 2019b), GW captures forming in GN (e.g., R. M. O'Leary et al. 2009), and few-body interactions in globular cluster (GCs; e.g., J. Samsing 2018) and AGNs (e.g., J. Samsing et al. 2022; G. Fabj & J. Samsing 2024) all give rise to eccentric mergers. The question in this case is therefore how do we tell the difference between the proposed dynamical channels (e.g., M. Arca Sedda et al. 2020; I. Romero-Shaw et al. 2022)?

In this paper, we explore and quantify an observable that can be used to distinguish eccentric BBH mergers formed dynamically through strong few-body interactions from those formed instead in near isolation, such as through single–single GW captures. The idea is that if a third object is nearby, as in the case of a binary-single mediated merger, the presence of this object will lead to modulations (dynamical and relativistic) in the observed GW-form that are not present, or cannot be trivially mimicked by, e.g., changing the BH mass and spin, in the GW-form of an isolated merging BBH. These modulations will, to the leading order, manifest as a phase shift in the observed GWs emitted by the eccentric binary, from which one in principle can infer the orbital evolution of all three interacting objects, in a similar way to what is done in the binary pulsar case (e.g., Y. Meiron et al. 2017; I. Romero-Shaw et al. 2023). This represents one of the only ways to probe the assembly mechanism of individual GW sources using GWs alone. In fact, a (circular) GW source observed by LVK might already show indications of GW phase shift, as was suggested by W.-B. Han et al. (2025) through a model-fit including line-of-sight (LOS) acceleration. Similar ideas have been presented for LISA-like sources, where the GW evolution time is long enough for a change in center-of-mass (COM) motion to be observed over the duration of the mission (e.g., N. Yunes et al. 2011; K. Inayoshi et al. 2017; T. Robson et al. 2018; K. Chamberlain et al. 2019; L. Randall & Z.-Z. Xianyu 2019; K. W. K. Wong et al. 2019; D. J. D'Orazio & A. Loeb 2020; N. Tamanini et al. 2020; A. Toubiana et al. 2021; V. Strokov et al. 2022; Z. Xuan et al. 2023; A. Laeuger et al. 2024; A. Tiwari et al. 2024). This line of models has recently been extended to include higher order general relativistic (GR) corrections and spin effects (e.g., F. Camilloni et al. 2023, 2024). A few papers have also explored the effect across several GW bands, including the LVK bands (e.g., A. Vijaykumar et al. 2023), but using simplified assumptions. However, the general case of dynamically assembled eccentric sources, including those forming naturally during chaotic scatterings in GCs (e.g., C. L. Rodriguez et al. 2018a; J. Samsing 2018), has not yet been consistently explored using dynamical prescriptions as the one we introduce in this paper. GW phase shift effects are not limited to dynamics alone, e.g., gas-drag and other dissipative effects will also give rise to their own unique GW perturbations (e.g., E. Barausse et al. 2014; L. Zwick et al. 2023).

With this motivation, we here present an exploration of how a third object perturbs and leads to shifts in the GW phase of a dynamically formed eccentric GW source from assembly to merger for both idealized and chaotic cases. This includes both an analytical solution, as well as a novel numerical post-Newtonian ($\mathcal{PN}$) framework that we use to directly quantify the nonlinear dynamical influence on the merging BBH from the perturber, and how this gives rise to unique GW phase shifts. Putting aside the observable challenges of eccentric sources, the basic questions we explore in this paper are under what mass scales, length scales, and timescales the GW phase shift is expected to be detectable, and if this could happen in real astrophysical systems. We further point out that the leading GW phase shift effect can be constrained using standard GW template matching using already existing template banks derived without these effects (e.g., W.-B. Han et al. 2025). The ongoing progress in developing waveforms for eccentric sources therefore holds a tremendous potential to not only identify dynamically assembled mergers but also learn about the exact few-body dynamics that brought the BBHs together.

2. Setup and Numerical Methods

Below, we introduce our setup, numerical methods, and describe what physical effects that generally result in GW phase shifts, as well as how this is dependent on the location of the observer.

2.1. Example and Setup

In this paper, we focus on BBH GW sources that form and evolve dynamically in 3-body systems, and to what degree the presence of the third object is able to modulate the observable GW signal emitted from the eccentric inspiraling BBH. To provide a clear understanding of the problem and its novel outcomes and observables, we start by considering the idealized and illustrative 3-body setup from Figure 1. This shows a “binary” BH consisting of BH1($m_1 = 5M_{\odot}$) and BH2 ($m_2 = 5M_{\odot}$) with initial semimajor axis (SMA), a_0, and eccentricity, e_0, on an outer circular orbit with radius R around

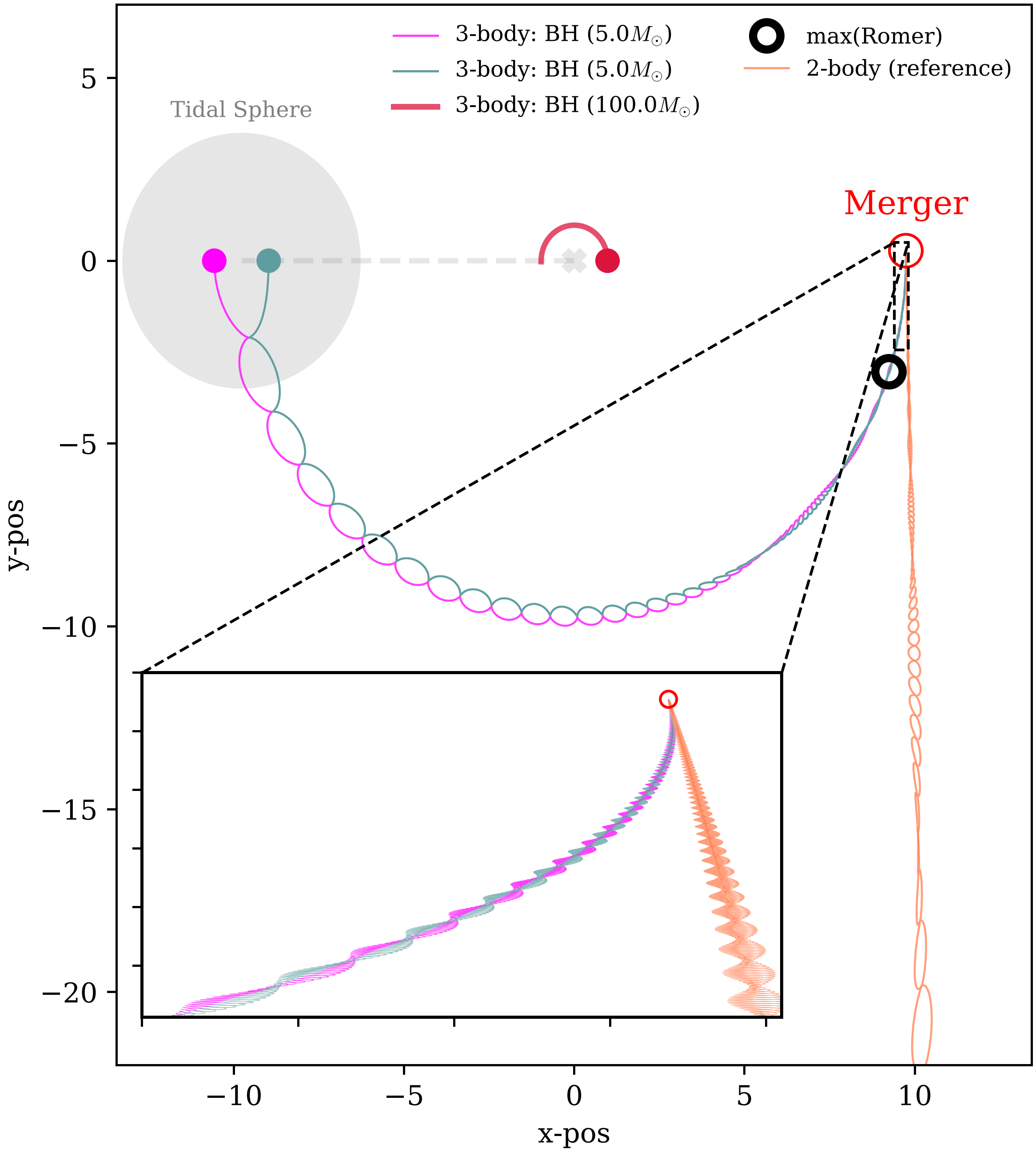

Figure 1. Evolution of a bound eccentric binary black hole merger: Evolution of a binary black hole (BH1,BH2) with masses $m_1 = m_2 = 5M_\odot$, orbiting a single black hole BH3 with mass $m_3 = 100M_\odot$ on a circular outer orbit with radius $R = 0.05$ au. The binary initially starts within the Hill sphere shown to the left (gray), after which it orbits BH3 for then to merge at the right at the point "Merger." Near merger is attached a "2-body-reference binary" (orange), which shows the evolution if the central BH3 is not present. This reference binary is generated by evolving the $\mathcal{PN}$-equations backwards in time from the point near merger, as further described in Section 2.3. We quantify the observable effects from the presence of BH3, by comparing the "3-body-perturbed binary" to this "2-body-reference binary," as further explained in Section 2.

a "perturber" denoted BH3($m_3 = 100M_\odot$). Here, and throughout the paper, we further assume the BHs have zero spin. We further denote the binary components "1" and "2," and the perturber by "3," often with a "BH" in front. The (BH1,BH2)-binary in Figure 1 is initiated within the binary Hill radius given by

$$R_{\rm H} \sim R((m_1 + m_2)/m_3)^{1/3}. \quad (1)$$

From this initial position, it orbits counterclockwise to finally merge, through the emission of GWs, after about half an outer orbit. In the following, we describe how we evolve such systems, and how to numerically extract the GW phase shift.

2.2. Numerical Methods

The numerical methods we use here and throughout the paper are based on the $\mathcal{PN}$-formalism (L. Blanchet 2006, 2014), where the N-body equations-of-motion (EOM) can be written in a "Newtonian way," where the inclusion of GR-effects is added to the Newtonian acceleration through a series-expansion in $(1/c)$, where c is the speed of light. Following the notation by

G. Kupi et al. (2006), the acceleration equation with the inclusion of $\mathcal{PN}$ terms can be written as

$$\underline{a} = \underbrace{\underline{a}_0}_{\text{Newt.}} + \underbrace{\underbrace{c^{-2}\underline{a}_2}_{1\mathcal{PN}} + \underbrace{c^{-4}\underline{a}_4}_{2\mathcal{PN}}}_{\text{precession}} + \underbrace{\underbrace{c^{-5}\underline{a}_5}_{2.5\mathcal{PN}}}_{\text{GW rad.}} + \mathcal{O}, \tag{2}$$

where $\underline{a}_0$ is the classical Newtonian acceleration term

$$\underline{a}_0 = \frac{Gm_2}{r^2}\underline{n}, \tag{3}$$

the following two terms, $\underline{a}_2$ and $\underline{a}_4$, are conservative terms leading to precession ($1\mathcal{PN}$, $2\mathcal{PN}$)

$$\begin{aligned}\underline{a}_2 = \frac{Gm_2}{r^2}(\underline{n}[-v_1^2 - 2v_2^2 + 4v_1v_2 + \frac{3}{2}(nv_2)^2\\ + 5\tfrac{Gm_1}{r} + 4\tfrac{Gm_2}{r}] + (\underline{v}_1 - \underline{v}_2)[4nv_1 - 3nv_2]),\end{aligned} \tag{4}$$

$$\begin{aligned}\underline{a}_4 \;=\; & \frac{Gm_2}{r^2}(\underline{n}[-2v_2^4 + 4v_2^2(v_1v_2) - 2(v_1v_2)^2\\ & + \tfrac{3}{2}v_1^2(nv_2)^2 + \tfrac{9}{2}v_2^2(nv_2)^2 - 6(v_1v_2)(nv_2)^2\\ & - \tfrac{15}{8}(nv_2)^4 + \tfrac{Gm_1}{r}(-\tfrac{15}{4}v_1^2 + \tfrac{5}{4}v_2^2 - \tfrac{5}{2}v_1v_2\\ & + \tfrac{39}{2}(nv_1)^2 - 39(nv_1)(nv_2) + \tfrac{17}{2}(nv_2)^2)\\ & + \tfrac{Gm_2}{r}(4v_2^2 - 8v_1v_2 + 2(nv_1)^2\\ & - 4(nv_1)(nv_2) - 6(nv_2)^2)]\\ & + (\underline{v}_1 - \underline{v}_2)[v_1^2(nv_2) + 4v_2^2(nv_1) - 5v_2^2(nv_2)\\ & - 4(v_1v_2)(nv_1) + 4(v_1v_2)(nv_2) - 6(nv_1)(nv_2)^2\\ & + \tfrac{9}{2}(nv_2)^3 + \tfrac{Gm_1}{r}(-\tfrac{63}{4}nv_1 + \tfrac{55}{4}nv_2)\\ & + \tfrac{Gm_2}{r}(-2nv_1 - 2nv_2)])\\ & + \tfrac{G^3m_2}{r^4}\left(\underline{n}\left[-\tfrac{57}{4}m_1^2 - 9m_2^2 - \tfrac{69}{2}m_1m_2\right]\right),\end{aligned} \tag{5}$$

and the last term, $\underline{a}_5$, is the leading term in the series that is dissipative ($2.5\mathcal{PN}$), which results in pairwise energy and angular momentum loss through the emission of GWs

$$\begin{aligned}\underline{a}_5 \;=\; & \frac{4}{5}\frac{G^2m_1m_2}{r^3}\Big((\underline{v}_1 - \underline{v}_2)[-(\underline{v}_1 - \underline{v}_2)^2\\ & + 2\frac{Gm_1}{r} - 8\frac{Gm_2}{r}]\\ & + \underline{n}(nv_1 - nv_2)[3(\underline{v}_1 - \underline{v}_2)^2\\ & - 6\frac{Gm_1}{r} + \frac{52}{3}\frac{Gm_2}{r}]\Big).\end{aligned} \tag{6}$$

In these equations, $\underline{a}$ denotes the acceleration vector of object "1" from object "2," m_i and $\underline{v}_i$ denote the mass and velocity vector of object "i," respectively, r is the scalar distance from object "2" to "1," $\underline{n}$ is the corresponding unit vector pointing from "2" to "1," and x_1x_2 denotes the dot-product of the two vectors $\underline{x}_1$ and $\underline{x}_2$. Note here that this pairwise acceleration must be evaluated in the COM of the two objects; the velocities are therefore relative to the pairwise COM. In the following sections, we discuss how to quantify the modulations caused by the third object, the role of the different $\mathcal{PN}$ terms, and what the main resultant observable effects are.

2.3. Comparing to a 2-body-reference Binary

To numerically quantify the effect from the nearby perturber, BH3, on the evolution and emission of GWs from the (BH1, BH2)-binary, we now introduce a *2-body-reference binary* defined as a binary with the same properties near merger as the 3-body-perturbed binary, but with a backwards trajectory from the time of merger that follows the evolution equations as if the perturbing BH3 was not present. In other words, our 2-body-reference binary refers to a normal unperturbed isolated GW inspiral between BH1 and BH2 that has the same properties right around merger as the 3-body-perturbed GW inspiral, but a different evolution as one goes backwards in time compared to the 3-body-perturbed binary evolution. To be able to make a correct comparison between our 3-body-perturbed binary and our 2-body-reference binary, we set the reference binary COM velocity vector to be the same as that of the perturbed binary right before merger. From this, we account for the trivial difference that could arise from the constant (longitudinal) Doppler shift, which also is not measurable due to its direct degeneracy with mass and redshift. Note that this way of quantifying differences by introducing a "reference binary" was also used in the theoretical arguments by Y. Meiron et al. (2017).

The "2-body-reference binary" is seen in Figure 1 with orange lines, and is calculated by simulating the (BH1,BH2)-binary backwards in time without BH3 from a point right before merger, by inverting the "time" and flipping the "sign" of the $2.5\mathcal{PN}$ radiation term. By now, comparing the 3-body evolution of the eccentric BBH around BH3 ("3-body (perturbed)") with the 2-body-reference binary evolution ("2-body (reference)"), as, e.g., seen in Figure 1, we can resolve the GW phase shift arising from the interplay between tidal couplings, $\mathcal{PN}$-terms, and the finite propagation speed of GWs giving rise to what is known as the Rømer delay (RDL), as is described in much greater detail in Section 3.3 and Figure 2.

2.4. Modulations of the GW Signal

Several effects can leave an imprint on the GW-form from the perturbed inspiraling BBH, compared to the isolated reference binary, including dynamics, Doppler effects, Shapiro- and GR time-delays, strong- and diffractive-lensing, as well as GW boosting (see Y. Meiron et al. 2017 for a compilation and comparison of some of these effects); however, in this paper, we restrict ourselves to first include and study the following two distinct effects:

1. *Dynamics*. Using our N-body code and novel numerical setup, we follow the Newtonian and post-Newtonian gravitational interactions between all objects, and from this keep track of how these couplings influence the evolution of the inspiraling BBH from assembly to merger. This dynamically perturbed evolution will show up as a GW phase shift.
2. *Rømer time-delay*. Since GWs propagate at the speed of light, the arrival time in the observer frame will depend on the orbital trajectory of the BBH source as it inspirals, which will give rise to a time-dependent GW phase shift. Using our $\mathcal{PN}$-body code, we derive this shift by comparing a 2-body-reference binary with our 3-body-perturbed binary.

The other effects listed above will occasionally also play a role, which depends not only on the system but also on the location of the observer. For example, the GR time-delay could play a role if the outer orbit has a significant eccentricity, as this time-delay essentially is a mapping of the potential difference the source experiences along its orbit. In addition, the observed delay from GR to the leading order will not depend on the position of the observer, and could therefore dominate over, e.g., Doppler effects that clearly are largest when observing in the same plane as the source is moving in.

In the limit where the inspiraling BBH is only moving a small fraction of its orbit around its perturber, the total GW phase shift as seen by a distant stationary observer, $\delta\phi$, can be approximated as (e.g., Y. Meiron et al. 2017)

$$\begin{aligned} \delta\phi &\approx \delta\phi_{\rm RDL} + \delta\phi_{\rm DYN} + \delta\phi_{\rm GR} \\ \delta\phi &\approx \Delta\phi_{\rm RDL} \times \cos(i)\sin(j) + \delta\phi_{\rm DYN} + \delta\phi_{\rm GR}, \end{aligned} \tag{7}$$

where $\delta\phi_{\rm RDL}$ is the GW phase shift from RDL as inferred by a distant observer, $\Delta\phi_{\rm RDL}$ is the *maximum possible* GW phase shift from RDL (see Figure 2), i is the angle in the plane of the "outer binary" (the binary composed of (BH1,BH2)+BH3) between the LOS of the observer and the line connecting the location of BBH merger and the COM of the 3-body system, j is the angle between the LOS and the angular momentum vector of the "outer binary," $\delta\phi_{\rm DYN}$ is the contribution from dynamics (*DYN*), and $\delta\phi_{\rm GR}$ refers to the remaining GR-effects (Shapiro delay, GR time-delay, etc.). In this work, we study the contributions $\delta\phi \approx \Delta\phi_{\rm RDL} \times cos(i)sin(j) + \delta\phi_{\rm DYN}$, and will in the remaining parts of the paper simply refer to the total GW phase shift seen by an observer by $\delta\phi$, and the maximum GW phase shift component from RDL by $\Delta\phi$.

2.5. Observers and GW Propagation

For studying and quantifying the GW phase shift induced by dynamics and RDLs (finite propagation speed of GWs), we consider an observer at a fixed location far away from the system: In all examples shown in this paper, we place the observer in the plane of the 3-body system along a line connecting the 3-body COM and the point of merger. We refer to this as the "observer." In terms of effects related to RDLs, this location will result in GW phase shifts that are close to the maximum possible value, i.e., $\delta\phi_{\rm RDL} \approx \Delta\phi_{\rm RDL}$, as we will show and describe later.

Numerically, for every spatial (x, y, z)-point evaluated by our N-body code along each binary trajectory ("3-body-perturbed" and "2-body-reference"), we propagate a "GW signal" from that point to the observer by taking into account that the GWs travel at the speed of light, c. Again, for this, we do not include possible GR wave scattering effects caused by the perturber (e.g., L. Dai et al. 2018), i.e., we assume the signal travels on straight lines between the source and the observer. This setup is also sketched out in Figure 2. In this way, we can follow and compare different quantities of the eccentric inspiraling BBH as a function of time in the rest frame of the observer, as will be shown below.

3. Numerical Results

In the following sections, we quantify the observable imprints on the binary GW signal from the presence of the BH perturber for our example shown in Figure 1, by systematically studying the difference between different quantities of the 3-body-perturbed binary and the 2-body-reference binary. This will also serve as a general explanation for how a perturber will give rise to a GW phase shift.

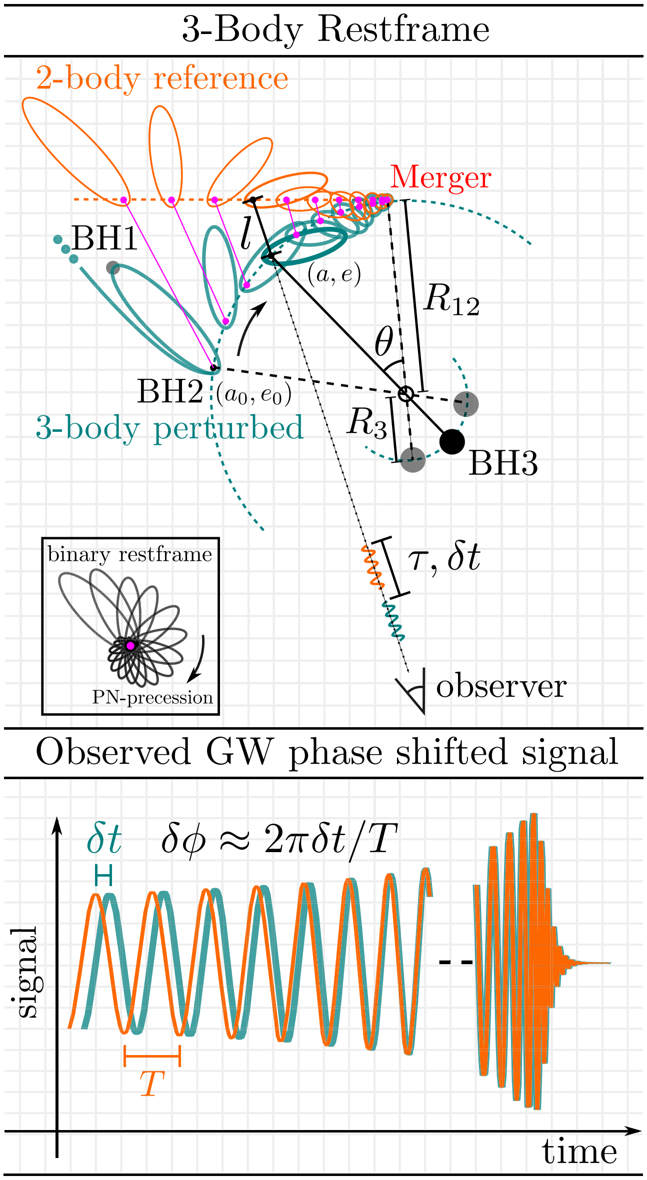

Figure 2. Time-delay and GW phase shifts. Top plot: Illustration of a (BH1, BH2)-binary, "3-body-perturbed," with initial elements a_0, e_0, orbiting a third object, BH3, until merger takes place at "Merger." At "Merger" is attached a reference binary (2-body-reference) representing the trajectory the (BH1,BH2)-binary would have taken if BH3 was not present (see Section 2.3). Several effects can cause the observed GW signal from the two evolutionary paths to differ (see Section 3.4), such as the effect from traveling on a curved- vs. a straight path, as shown here. The two paths differ by a maximum distance l (pink lines) that gives rise to a maximum time shift $\tau = l/c$, which manifests as an observed value δt. Bottom plot: Illustration of the 3-body-perturbed and 2-body-reference GW signals, respectively. The two signals are displaced relative to each other, which is what is referred to as the GW phase shift. This shift can be approximated by $\delta\phi(t) \approx 2\pi\delta t(t)/T(t)$, where $T(t)$ is the orbital period of the reference binary, as further described in Section 3.4.

3.1. Tidal Perturbations of Binary Elements

The first quantities we study are the SMA and eccentricity of the inspiraling BBH, and how the tidal influence of BH3 affect these orbital elements as a function time in the rest frame of the binary, i.e., without any propagation effects including RDLs. For this, we now consider Figure 3, which shows from top to bottom the difference between the orbital elements of the 3-body-perturbed binary and the 2-body-reference binary in terms of the relative change in SMA ($a_{3b}/a_{2b} - 1$), eccentricity

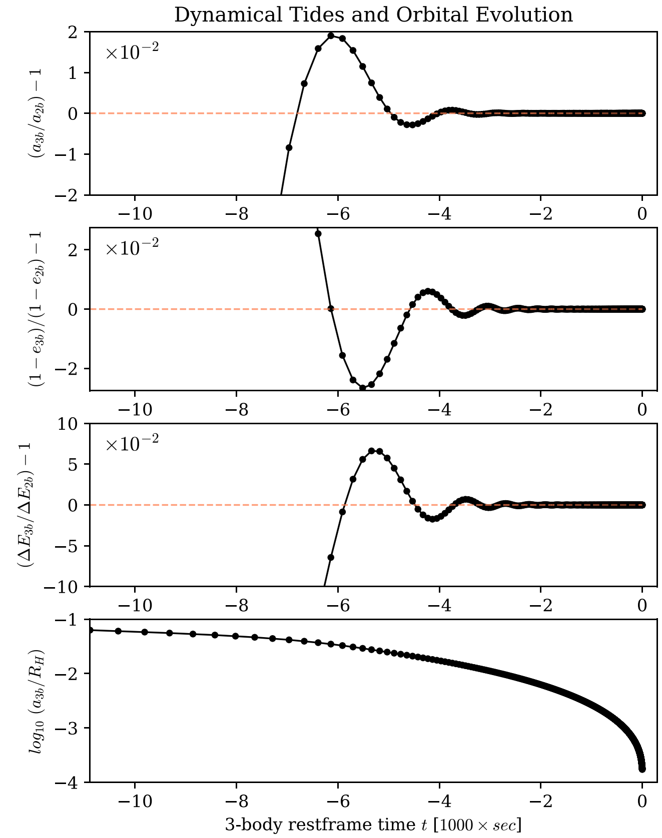

Figure 3. Change in orbital elements from tides. The figures shows data from the illustrative setup presented in Figure 1, of a [$5M_{\odot}$, $5M_{\odot}$] BBH orbiting a $100M_{\odot}$ BH perturber. Counting from top to bottom: Panel (1), relative difference in SMA between the 3-body-perturbed binary (a_{3b}) and the 2-body-reference binary (a_{2b}), as a function of time. Panel (2), relative difference in eccentricity as a function of time. Panel (3), corresponding relative difference in GW energy radiated at pericenter, $\Delta E_{3b}/\Delta E_{2b} - 1 = (r_{3b}/r_{2b})^{-7/2} - 1$ (see Equation (39)), where $r = a(1 - e)$ is the pericenter distance. Panel (4), SMA of the 3-body-perturbed BBH relative to the Hill sphere (see Equation (1)). All orbital quantities have here been estimated using the geometric method, as further explained in Section 3.1 and shown in Equation (8).

$((1 - e_{3b})/(1 - e_{2b}) - 1)$, GW energy radiated at pericenter $(\Delta E_{3b}/\Delta E_{2b} - 1)$, and the SMA relative to the binary Hill sphere, (a_{3b}/R_H), for the system presented in Figure 1. Here, the subscripts $3b$ and $2b$ refer to the 3-body-perturbed binary and 2-body-reference binary, respectively. The SMA and the eccentricity, a and e, shown here are estimated using a geometric method that is based on knowing the position of the interacting objects as a function of time, such that a and e can be estimated as

$$\begin{aligned} a &= (r_a + r_p)/2 \\ e &= 1 - r_p/a \end{aligned} \tag{8}$$

where r_a and r_p are the apocenter and pericenter distance of the time-evolving BBH orbit, respectively, that we measure using our N-body code. In fact, the Newtonian orbital elements, a and e, can be very difficult to even properly define for strong precessing and decaying binaries, and can as a result lead to biased results (e.g., L. Zwick et al. 2020; A. Tucker & C. M. Will 2021; A. Ciarfella et al. 2022; A. Bonino et al. 2023; M. A. Shaikh et al. 2023).

Considering Figure 3 in more detail, we see a clear wavy modulation in both the change of a and e that is due to tidal couplings between the (BH1,BH2)-binary and the single BH3. The corresponding time-evolving modulation period directly corresponds to the $1\mathcal{PN}+2\mathcal{PN}$ orbital precession period of the (BH1,BH2)-binary. The reason is that the tidal coupling between the (BH1,BH2)-binary and the BH3-single depends not only on the BBH SMA relative to the Hill sphere (bottom panel) but also on the BBH orbital orientation relative to the perturber, which to the leading order will change on a timescale equivalent to the BBH precession period (see also A. S. Hamers & J. Samsing 2019; J. Samsing et al. 2019).

The $1\mathcal{PN}+2\mathcal{PN}$ orbital precession period is therefore imprinted in the time-evolving orbital elements, which propagates to the inspiral time of the binary through changes in the GW energy radiated at pericenter, which finally shows up as an observable GW phase shift.

Besides the observational opportunities of indirectly observing the wavy modulations in the orbital elements through the GW signal, the most important indirect effect of the $\mathcal{PN}$-precession is essentially to average out any potential gradual energy exchange from tides on the (BH1,BH2)-binary (see, e.g., J. Samsing et al. 2019). In other words, this averaging effect from $\mathcal{PN}$-precession will protect the binary from experiencing a runaway change in a, e through, e.g., repeatedly expanding the binary through tidal pumping over each orbit, which would otherwise result in a greater and greater unphysical large GW phase shift between the 3-body-perturbed and the 2-body-reference GW signal (a toy model of this type was explored in I. Romero-Shaw et al. 2023 mainly for demonstrating new inference methods). In the Appendix, we illustrate this, by showing simulations of a system similar to the one presented in Figure 1, but without the $1\mathcal{PN}$, $2\mathcal{PN}$ precession terms included. This results in a clear, systematic incorrect evolution of the binary and thereby GW phase shift.

Below, we continue by considering how these tidal effects and the additional effect from RDLs give rise to modulations in the GW peak frequency and a GW phase shift.

3.2. GW Peak Frequency Modulations

To explore the observable GW effects resulting from the presence of the perturbing BH3, we start by considering the top panel in Figure 4, which shows the GW peak frequency f_p of the inspiraling (BH1,BH2)-binary approximated as

$$f_p \approx \frac{1}{\pi}\sqrt{Gm_{12}/r_p^3}, \tag{9}$$

where $m_{12} = m_1 + m_2$, and r_p is the pericenter distance, as a function of time. The blue and the orange lines show results for the 3-body-perturbed and the 2-body-reference BBHs, respectively. In the figure, each dot corresponds to the time of pericenter passage and illustrates at what points in time one would see a GW burst when the source is still highly eccentric.

One can interpret this time series of pericenter passages as a clock that represents the evolution of the binary as a function of time. In the well-studied case of binary pulsars, one uses the time-modulation in the pulsar arrival times to infer information about the system. Our "burst-clock" case is equivalent, as the GW burst modulations in both frequency and arrival time carry imprints of the environment the binary inspirals within.

The first feature we see in the GW peak frequency f_p plot is (again) a clear wavy modulation, which directly results from

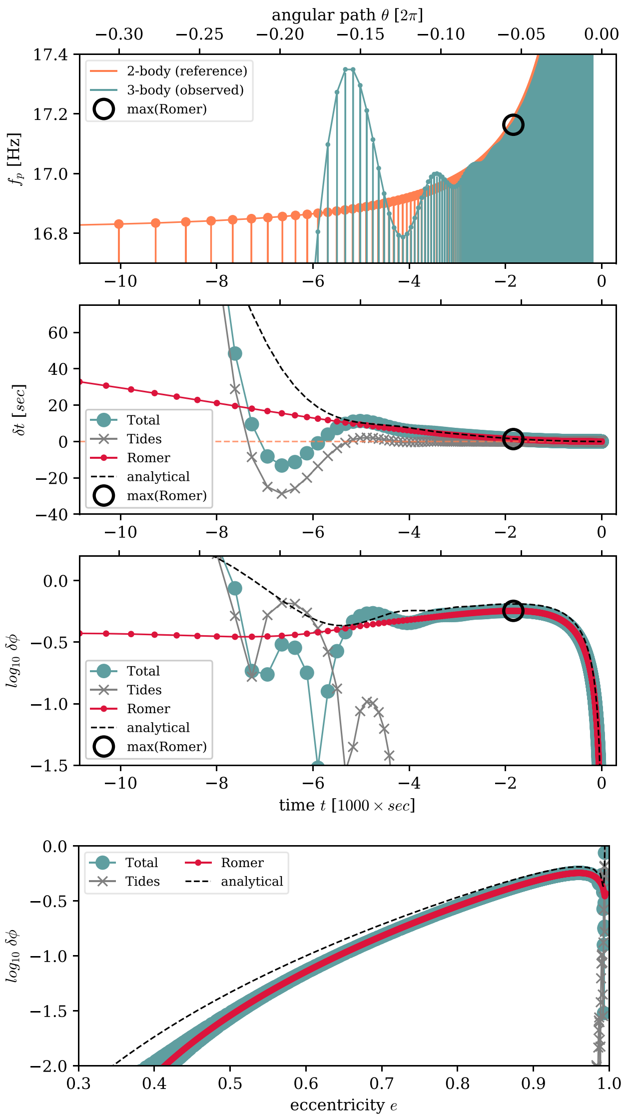

Figure 4. Differences in observed GW signal. Observable differences between the "3-body-perturbed" (BH1,BH2)-binary and the "2-body-reference" binary shown in Figure 1, and discussed in Section 2.2. Counting from top to bottom: Panel (1), GW peak frequency f_p as a function of time for the perturbed BBH (3-body (observed)) and the reference BBH (2-body (reference)). Panel (2), difference in arrival time seen by the observer , δt, of the GWs sent out at each pericenter passage, by the orbiting binary and the reference binary, respectively, as a function of time t. Panel (3), the time-difference converted to GW phase shift, $\delta\phi$, as further described in Section 3.4 and 4.2. Panel (4), GW phase shift, $\delta\phi$, as a function of the (BH1,BH2)-binary eccentricity. The red and gray lines show the contribution from Rømer delay (time-dependent Doppler shift) and dynamical tides (dynamical interactions), respectively, where black dashed lines show our full analytical solutions presented in Section 4.

the periodic tidal influence on the (BH1,BH2)-binary orbital elements from BH3, as we described in Section 3.1. Besides information from the GW phase shift, one can in principle also put further observable constraints on the system if the GW peak frequency f_p modulation is observed; however, the modulation is naturally largest at early times when the SMA of the binary is still large enough for the tidal couplings to be strong enough. It is therefore questionable if these modulations have observational opportunities, as this will require accurately detecting the first few peaks of the signal. On the other hand, one should note that the modulations in f_p are independent of the observer location, whereas effects from, e.g., RDL in principle can be undetectable if the BBH is observed face-on relative to its orbit around the BH3-perturber.

3.3. *Rømer Delays along the Orbit*

We now consider the second panel in Figure 4, which shows the difference in seconds, δt, in the time of arrival of the GW signal emitted by the 3-body-perturbed BBH and the 2-body-reference BBH, respectively, as seen by the observer (see Section 2.5). The time has here been shifted such that $\delta t = 0$ at merger by definition (see also Y. Meiron et al. 2017). Technically, for both the 3-body-perturbed binary and the 2-body-reference binary, we record the position and time of all pericenter passages (time and location of all peaks in f_p, which we consider as our "clock") in the rest frame of each respective binary, after which we propagate these time series to the position of the observer. In the observer rest frame, we then take the time difference between the time series from the 3-body binary and the 2-body-reference binary, respectively, which gives us δt. In other words, δt is the light travel time (projected along the LOS of the observer) between the 3-body-perturbed binary COM-trajectory (curved trajectory) and the 2-body-reference binary COM-trajectory (linear trajectory) as a function of observer time, t, as also shown in Figure 2 (note that τ in this figure denotes the actual light travel time and not the projected along the observer LOS; for our chosen position of the observer, these two timescales are near identical). This is also what is referred to as the RDL.

The observed time difference δt can in general be due to several physical effects. For illustrative purposes, we split in the figure the computationally measured δt, denoted "Total" (blue), into its two contributions; tides (gray) and RDL (red). The "tides"-contribution arises from perturbations to the orbital elements of the 3-body binary that is not present in the 2-body-reference binary (see Section 3.1), where the "Rømer delay"-contribution is due to the BBH inspirals along a curved orbit (around BH3) versus a straight line (unperturbed). As seen in the second panel in Figure 4, tides greatly dominate at early times of the inspiral, which is expected as this is when the BBH is still wide enough to be in tidal contact with the third object. The difference from the 2-body-reference evolution is large, which in principle would give rise to major hints that something nearby is perturbing; however, observing the first few peaks during the early stages when the eccentricity is still very high is extremely difficult, and will therefore not be the main interest of this paper. Focusing at times closer to merger, we see that RDL starts to dominate, essentially because the tidal contribution quickly fades away. The actual time difference is getting smaller and smaller, but this is not necessarily the same as the GW phase shift, which is the quantity that effectively tell us if these effects can be observed or not. Finally, the oscillating behavior in δt is again a direct consequence of the $1\mathcal{PN}+2\mathcal{PN}$-precession terms coupling to tides; hence, it is clear that δt caused by tides does not just gradually build up as a function of time (see also our Appendix).

3.4. *GW Phase Shifts*

The third panel in Figure 4 shows the GW phase shift $\delta\phi$ between the 3-body binary and the 2-body-reference binary as seen by the observer. This can be approximated by the observed difference in number of orbital cycles between the

3-body-perturbed signal and the 2-body unperturbed reference signal times 2π, to convert the orbital count difference to a shift in radians. As we illustrate later, this is indeed the phase shift of the GW-form in the limit where the (BH1,BH2)-binary is circular (except for a trivial factor of 2).

In our numerical framework, we estimate the GW phase shift by taking the difference in arrival time between the 3-body-perturbed and 2-body-reference binary GW signals in the observer frame, δt, and divide this by the corresponding orbital time of the 2-body-reference binary, T(t), that we measure numerically from the f_p-peak time locations. This fraction we then multiply by 2π to get the GW phase shift, such that $\delta\phi \approx 2\pi\delta t/T(t)$.

This is also explained in Figure 2. Again, for illustrative purposes, we have in Figure 4 separated the contributions to $\delta\phi$ from tides and RDL. Note that the true GW phase (connected to the evolution of the true anomaly that evolves nonlinearly in time) is not easily measured when the binary is highly eccentric, in which case the evolving GW signal is closer to a series of bursts. For this reason, we keep our definition of GW phase shift even when the binary is eccentric. These technical issues will naturally not arise when working with real or numerical relativity generated waveforms.

Considering further the results for $\delta\phi$ shown in Figure 4, we see that if we track the binary backwards from merger ($t = 0$) toward the time of assembly, the phase shift $\delta\phi$ first increases, as expected from earlier studies in the $e = 0$ limit (Y. Meiron et al. 2017), but does not continue to grow as e increases, i.e., as we go backwards in time. Instead, it levels off and gradually decreases again, until it reaches a region where tides start to dominate (the gray lines start fluctuating above the red line). As we will analytically prove below, this shape of $\delta\phi$ is unique to eccentric GW sources orbiting around other objects. In short, the reason why it levels off can be put as follows. First, we note that, at a given time t, the binary will be at a given location on the outer orbit and thereby have a given value for $\delta t(t)$, which is a purely geometric factor that has nothing to do with the evolution of the inner binary. However, the orbital time of the inner binary, $T(t)$, that relates to $\delta\phi$ as $\sim\delta t/T(t)$ evolves by itself as a function of t depending on the properties of the binary and more generally on the dissipative force (gas-drag, GW radiation, etc.). For GW radiation, the eccentric limit corresponds to a larger $T(t)$ at a given time t compared to if the binary was circular, which then leads to a relatively smaller $\delta\phi$ compared to the circular case. That the GW phase shift first increases (circular limit) after which it decreases (eccentric limit) naturally gives rise to a peak in $\delta\phi$ in the RDL dominated region, which we have highlighted with a black circle (Figure 4). This peak position is also shown in Figure 1 with a black circle, from which we see how close to merger the RDL peak is compared to the full orbital trajectory. The exact location of the peak naturally depends on the exact position of the observer. What we show here is very close to the optimal case. The trivial dependence on the observer position will not be addressed in this paper, as our main focus will be on first quantifying the intrinsic and unique parts of the GW phase shift signal before the observer is factored in.

Finally, we have in the bottom panel of Figure 4 plotted the phase shift $\delta\phi$ as a function of the evolving BBH eccentricity, e. (note that the binary here evolves from right to left). As seen, once the BBH eccentricity e reaches a value of ≈0.95, the GW phase shift caused by RDL is at its maximum. That the GW phase shift peaks at an eccentricity significantly below the eccentricity at formation ($e_0 \sim 0.9999$) is encouraging, as the lower the eccentricity is, the less challenging the observations will be (e.g., M. Zevin et al. 2021b). Below, we explain all these results using analytical arguments, from which we will see how especially the GW phase shift depends on time, eccentricity, mass scales, and length scales.

4. Analytical Solution

In this section, we present the first analytical solution to the time-evolving GW phase shift resulting from RDL, which relates to the nonrelativistic Doppler shift, of an eccentric BBH inspiraling along an orbit around a third BH.

4.1. Assumptions and Setup

We assume the outer orbit, i.e., the orbit of the BBH (GW source) around the single BH (perturber), is circular to get a clear picture for how the mass scales, length scales, and timescales of the problem influence the magnitude and general evolution of $\delta\phi$. The more general case with an eccentric outer orbit will be studied in upcoming work. The setup and notations we use here are explained in Figure 2. In this figure, the center is at the COM of the 3-body system; $R = R_{12} + R_3$ is the distance between the BBH and the single BH, which is a sum of the distance from the BBH, R_{12}, and the single BH, R_3, to the 3-body COM, respectively. The inspiraling BBH has an initial SMA a_0, and eccentricity e_0, from which it evolves toward the point of merger, which is denoted by "Merger" in the figure. Without a loss of generality, we take the time at this point to be $t = 0$, such that the time t is equivalent to the merger time, t_m. To every value of t, there exists a value for the angle, θ, which denotes the angular evolution of the BBH around the 3-body COM with respect to the point of merger as illustrated in Figure 2. As was seen numerically in Figure 1, the most important part of the GW phase shift caused by RDL is created relatively close to merger, which is when θ is small, and we will therefore in our analytical calculations assume that $\theta \ll 1$, as described further below.

Using this setup, we now calculate the evolving *maximum* GW phase shift from RDL, $\Delta\phi$, as described in Equation (7). With our choice of observer (see Section 2.5), the observed contribution from RDL in the limit $\theta \ll 1$ is identical to the maximum value, $\Delta\phi$, we derive here. The observed value $\delta\phi$ and the maximum value $\Delta\phi$ can therefore be compared directly as we will do in the following.

4.2. General Relations

To estimate $\Delta\phi$ at each point along the trajectory of the BBH around the perturbing BH, we first imagine that we observe a GW burst from the 3-body-perturbed BBH at some time t, with corresponding angle $\theta(t)$. This GW burst is separated in time compared to a GW burst sent out from the 2-body-reference BBH by an amount τ, where τ is the light travel time between the 3-body-perturbed binary COM position and the 2-body-reference binary COM position at time t (pink lines in Figure 2). This manifests as the Rømer GW phase shift. To see this, we continue by noting that the distance between the 3-body and 2-body COM positions at time t, denoted here by l

as also shown in Figure 2, can be written as

$$\begin{aligned} l &= 2R_{12}[(\theta/2)^2 + \sin^2(\theta/2) \\ &\quad -2(\theta/2)\sin(\theta/2)\cos(\theta/2)]^{1/2} \\ &\approx 2R_{12}(\theta/2)^2, \quad (\theta \ll 1), \end{aligned} \tag{10}$$

where in the last equality we have expanded to the leading order in θ (our considered limit $\theta \ll 1$). By now, using that the angle θ can be written as

$$\theta(t) = \frac{v_{12}t}{R_{12}}, \tag{11}$$

where v_{12} is the COM velocity of the binary relative to the 3-body COM,

$$v_{12} = \frac{m_3}{M}\sqrt{\frac{GM}{R}}, \tag{12}$$

we now find that the corresponding light travel time, $\tau = l/c$, can be written as

$$\tau(t) = \frac{l(t)}{c} = \frac{1}{2}\frac{Gm_3}{c}\frac{t^2}{R^2} \tag{13}$$

where we have used that $m_{12}v_{12} = m_3v_3$, $m_{12}R_{12} = m_3R_3$, and defined $M = m_1 + m_2 + m_3$. This quadratic dependence on time t is seen in Figure 2, where $\delta t \approx \tau$ given our choice of observer, which fits our simulations when $\theta \ll 1$, or equivalently where t approaches 0 (black dashed line). Note that the normalization of τ scales as $1/R^2$, which indicates that the largest time shifts at a given t and in the $\theta \ll 1$ limit, will be found for the most compact binaries.

With our derivation of τ, we can now estimate the corresponding GW phase shift $\Delta\phi$, which can be written as

$$\begin{aligned} \Delta\phi(t) &\approx 2\pi\tau(t)/T(t), \\ &\approx \frac{1}{2}\frac{G^{3/2}}{c}\frac{m_3 m_{12}^{1/2}}{R^2} \times \frac{t^2}{a(t)^{3/2}} \end{aligned} \tag{14}$$

where we have used Equation (13), and the orbital time of the BBH at time t can be estimated as

$$T(t) = 2\pi\sqrt{a(t)^3/Gm_{12}}. \tag{15}$$

As seen in Equation (14), the last term, $t^2/a(t)^{3/2}$, only depends on the binary properties, and we can therefore conclude that $\Delta\phi$ will, regardless of the eccentricity of the binary, scale $\propto R^{-2}$. As we are considering the $\theta \ll 1$ limit, this R is essentially a measure of curvature, acceleration, or how much the orbital velocity vector changes in time, i.e., $\dot{v}_{12}$ (N. Yunes et al. 2011).

If we assume that the BBH SMA, $a(t)$, scales with time as $a(t) \propto t^{\alpha}$, one finds that

$$\Delta\phi(t) \propto t^{2-3\alpha/2}, \quad (a \propto t^{\alpha}), \tag{16}$$

from which one can define a critical α defined as

$$\alpha_c = 4/3, \quad (a \propto t^{\alpha}). \tag{17}$$

As seen, if $\alpha < \alpha_c = 4/3$, then $\Delta\phi(t)$ will increase with time t, whereas, if α changes from being $< \alpha_c$ to $> \alpha_c$ along the BBH evolution, then $\Delta\phi$ will start to decrease. This is exactly what we see in the case when the BBH transitions from its approximate circular state ($\alpha \approx 1/4$) around merger, to its earlier highly eccentric state ($\alpha \approx 2$), as further explained in the following.

4.3. Evolution with Time

To gain further analytical insight into $\Delta\phi$ as a function of time t, we have to consider the BBH $e = 1$ and $e = 0$ limits separately, as no full analytical solution is formally possible as a function of $t(e)$. A closed form analytical solution is on the other hand possible as a function of $e(t)$ as shown later in Section 4.4.

4.3.1. Circular Limit ($e = 0$)

Starting with the well-studied $e = 0$ limit (circular-orbit binary evolving around a perturber on a circular orbit—see, e.g., N. Yunes et al. 2011; Y. Meiron et al. 2017), we first use the expression for the merger time in the circular case t_c from P. C. Peters (1964)

$$t_c = (5/256)(c^5/G^3)a^4 m_1^{-1} m_2^{-1} m_{12}^{-1}, \tag{18}$$

and substitute it into Equation (14), which leads us to

$$\Delta\phi(t) \approx \frac{c^{7/8}G^{3/8}}{2}\left(\frac{5}{256}\right)^{3/8} \times \frac{m_3}{R^2}\frac{m_{12}^{1/8}}{m_1^{3/8}m_2^{3/8}} \times t^{13/8}. \tag{19}$$

From this, we see that $\Delta\phi \propto t^{13/8}$ ($e = 0$), which explains the rapid increase in $\Delta\phi$ we see in panel (3) in Figure 4. Considering the case where $m_1 = m_2$, the above Equation (19) reduces to $\Delta\phi \propto m_3 R^{-2} m_{12}^{-5/8} t^{13/8}$. From this, we see that $\Delta\phi$ generally is largest for high perturber mass m_3, small outer orbital radius R, and small binary masses.

4.3.2. Eccentric Limit ($e = 1$)

As we are going backwards in time from the point of merger, the binary eccentricity increases until it reaches its initial eccentricity $e_0 \sim 1$. We now consider the solution in this limit. For this, we make use of the solution to the merger time in the eccentric limit from P. C. Peters (1964), which can approximated by

$$t_e \approx t_c \times (768/425)(1 - e^2)^{7/2}, \tag{20}$$

where t_c is given by Equation (18). By now, using the identity $(1 - e^2) = (1 - e)(1 + e)$, and the definition of the pericenter distance, $r_p = a(1 - e)$, the merger time can be written as

$$t_e \propto a^{1/2} r_p^{7/2}. \tag{21}$$

The radiation of angular momentum is much smaller than the radiation of energy, which leads to the result that the pericenter distance remains nearly constant during the eccentric phase of the inspiral. From this, one concludes that the merger time in the $e \sim 1$ limit approximately scales as $t_e \propto a^{1/2}$. This implies that in the $e = 1$ limit, α, defined in Equation (16), takes the value $\alpha = 2$, which leads to

$$\Delta\phi(t) \propto t^{-1}. \tag{22}$$

This means that, when the binary starts to have a significant eccentricity, the GW phase shift will start to decrease again after having increased to a nonzero value during the $e \approx 0$ phase. This $\propto t^{-1}$ dependence is also confirmed using our simulations shown in Figure 4, as also discussed in Section 3.4. Note that we have not added any normalization and scaling factors in the above relation, as it has to be bridged to the $e \approx 0$ solution. Below, we illustrate how one can describe the GW phase shift $\Delta\phi$ and its scalings, across the entire range of eccentricity e by writing $\Delta\phi$ as a function of e instead of t.

4.4. Evolution with Eccentricity

To derive a solution for $\Delta\phi$ valid for all e, we start by recalling the relation between a and e given by P. C. Peters (1964)

$$a(e) = \frac{C_0 e^{12/19}}{(1 - e^2)} \times g(e), \tag{23}$$

where

$$g(e) = (1 + 121e^2/304)^{870/2299}, \tag{24}$$

and C_0 is a constant that depends on the initial conditions, a_0, e_0. In the case of dynamical assembly, the BBH will start with high eccentricity $e_0 \approx 1$, from which it trivially follows that the constant $C_0 \approx 2r_0/g(1)$, where $r_0 = a_0(1 - e_0)$. With this constant, we can now write the relation $a(e)$ as

$$a(e) \approx \frac{2r_0 e^{12/19}}{(1 - e^2)} \frac{g(e)}{g(1)}, \quad (e_0 \approx 1). \tag{25}$$

By now, substituting this $a(e)$ into our general expression for $\Delta\phi$ given by Equation (14), with t being the merger time in the eccentric limit from Equation (20), one can write the following two useful expressions for $\Delta\phi$, as a function of r_0 and f_0, respectively, that depend only on e

$$\begin{aligned}\Delta\phi(e) \approx\ & \frac{288\sqrt{2}}{85^2 g(1)^{13/2}} \frac{c^9}{G^{9/2}} \times \frac{m_3}{R^2} \frac{r_0^{13/2}}{m_1^2 m_2^2 m_{12}^{3/2}} \\ & \times e^{78/19}(1 - e^2)^{1/2} g(e)^{13/2} \\ \approx\ & \frac{288\sqrt{2}\pi^{-13/3}}{85^2 g(1)^{13/2}} \frac{c^9}{G^{7/3}} \times \frac{m_3}{R^2} \frac{m_{12}^{2/3}}{m_1^2 m_2^2} \times f_0^{-13/3} \\ & \times e^{78/19}(1 - e^2)^{1/2} g(e)^{13/2},\end{aligned} \tag{26}$$

where for the last relation we have used Equation (9). As seen here, the dependence on e factors out into the function

$$F(e) = e^{78/19}(1 - e^2)^{1/2} g(e)^{13/2}, \tag{27}$$

meaning that the functional shape of the GW phase shift $\Delta\phi$ as a function of e has a unique form, where the BH masses, outer orbital radius, and initial conditions for the BBH inspiral only act as scaling factors to this general form. This solution is overplotted with the numerical results shown in Figure 4 in the bottom panel, from which we see excellent agreement within our approximation (at low eccentricity, the analytical model deviates slightly, as our framework is derived using the eccentric BBH merger inspiral time). The function $F(e)$ itself is illustrated in Figure 5.

This analytical solution for $\Delta\phi(e)$ serves as one of our main results, as it represents the first closed form solution to the question of what the GW phase shift is of an eccentric binary orbiting and merging around a third object.

4.5. Evolution with Frequency

It is useful to consider $\Delta\phi$ as a function of GW frequency, f, as this is naturally closely connected to observational constraints. For example, if the GW source initially forms outside the observable band, i.e., at lower frequencies, one would like to know what the GW phase shift is once the source enters the band, i.e., passes some characteristic frequency. To link our work with earlier studies, we first write out $\Delta\phi$ as a function of f assuming the BBH is inspiraling with $e = 0$ during its entire evolution. Using Equation (9) and Equation (18), we can now rewrite Equation (19) as

$$\begin{aligned}\Delta\phi(f, e = 0) \approx\ & \frac{c^9 G^{-7/3}}{2\pi^{13/3}} \left(\frac{5}{256}\right)^2 \\ & \times \frac{m_3}{R^2} \frac{m_{12}^{2/3}}{m_1^2 m_2^2} \times f^{-13/3}.\end{aligned} \tag{28}$$

This is exactly the same expression as the one derived in Y. Meiron et al. (2017; Section 4.1), including the prefactor, that, in the same units and notation as in Y. Meiron et al. (2017), here takes the form $8\pi^{-13/3}(5/256)^2 c^9 G^{-7/3} M_{\odot}^{-7/3} R_{\odot}^{-2} 10^{-13/3} \approx 446$ (except for an expected factor of 2, as we consider the phase shift in terms of binary orbital periods to make it possible to smoothly transition from the eccentric to the circular limit, where Y. Meiron et al. 2017 naturally define it in terms of GW cycles). This consistency serves as an excellent check of our entire approach and numerical framework.

In the general $e > 0$ case, a closed form solution between $\Delta\phi$ and f is impossible, as e cannot be written as a function of f, as we will explain below. However, we can still get insight into this after a few approximations. For this, we start by combining Equations (25) and (9), to find how the GW peak frequency changes as a function of eccentricity as the binary spirals in

$$(f/f_0)^{2/3} \approx \frac{(1 + e)}{2e^{12/19}} \frac{g(1)}{g(e)}, \tag{29}$$

where f_0 denotes the GW peak frequency at assembly. By now, taking this expression to the power of 13/2, one can rearrange the above equations as $f^{-13/3}(1 + e)^7 2^{-13/2} = f_0^{-13/3} e^{78/19}(1 + e)^{1/2}(g(e)/g(1))^{13/2}$. This relation can now be substituted into Equation (26), from which we find

$$\Delta\phi(f) \approx \Delta\phi(f, e = 0) \times H(e), \tag{30}$$

where $\Delta\phi(f, e = 0)$ is given by Equation (28), and $H(e)$ is given by

$$H(e) = (1 + e)^7(1 - e)^{1/2}. \tag{31}$$

Ultimately, we wanted this to be as a function of frequency f only, but e cannot be isolated algebraically as a function of f. However, the above relations tell us that in general the GW phase shift of an eccentric binary does not take a simple power-law form as a function of f; instead, it will have unique features that depend strongly on the binary eccentricity, e, which is connected to the frequency evolution. More specifically, when going backwards from the point of merger, the term $H(e) = (1 + e)^7(1 - e)^{1/2}$ will increase until e reaches the value $e_H = 13/15 \approx 0.9$ (the value that maximizes $H(e)$), after which $H(e)$ will strongly fall toward 0 when $e = e_0 \sim 1$, i.e., when $f \sim f_0$. That is, the GW phase shift will increase faster than the circular $f^{-13/3}$ when the binary is eccentric, until $e \sim 0.9$, after

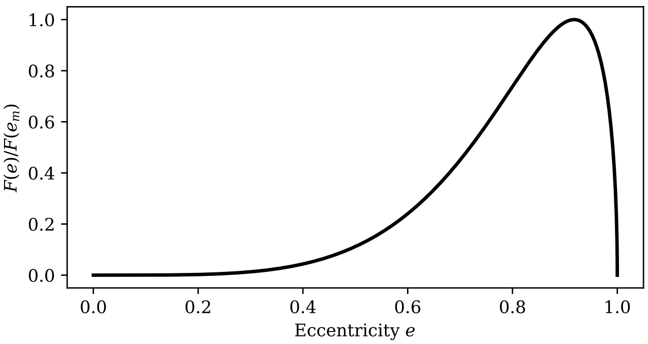

Figure 5. GW phase shift and eccentricity: The figure pictures Equation (27), which represents our analytically derived universal relation between the GW phase shift, $\delta\phi$, and the eccentricity, e, of the BBH as it inspirals from its initial value $e_0 \sim 1$ all the way to merger at $e \sim 0$. The curve has been normalized to its peak value, and illustrates therefore the general factor the GW phase shift scales by when the eccentricity changes in time (here, going from right to left). Interestingly, this scaling only depends on eccentricity, and not on the BH masses or length scales. Note that the trivial factor from the position of the observer has not been factored in; the figure therefore illustrates an upper limit as a function of eccentricity.

which it quickly declines (note that where $H(e)$ peaks is not necessarily where $\Delta\phi$ peaks as will be clear in Section 4.6 below). At its maximum,

$$H(e_H) = (1 + 13/15)^7(1 - 13/15)^{1/2} \approx 30, \tag{32}$$

which tells us that, for most of the inspiral, the GW phase shift of an eccentric binary will be *larger* than a circular binary with the same GW frequency, by up to a factor of $\sim$30 at its peak. Whether this means that future 3G GW detectors are more sensitive to GW phase shifts in such inspirals will be topics of future work, as the correct signal-to-noise ratio (SNR) has to be factored in.

A crude approximation makes it possible to get a rough estimate for how $\Delta\phi(f)$ scales with frequency only, without the eccentricity dependence as we have above. To see this, we consider the $e \approx 1$ limit for which we can write Equation (29) as $(f/f_0)^{-2/3} \approx e^{12/19}$, which leads to $e \approx (f_0/f)^{19/18} \approx (f_0/f)$. Now, plugging this into Equation (30), we find the following approximate relation

$$\Delta\phi(f) \approx \Delta\phi(f, e = 0) \times (1 + (f_0/f))^7(1 - (f_0/f))^{1/2}. \tag{33}$$

Figure 6 shows our considered different solutions, together with the results from the system introduced in Figure 1. As seen, our approximate analytical solutions (Equation (30), pink; and Equation (33), black) correctly capture both the shape and the normalization of the GW phase shift from f_0 and above, where our considered RDL dominates. The deviations around f_0 and below are coursed by the tidal perturbations to the binary, which dominate at early times until the BBH hardens enough for RDL to take over (see also Figure 4). On the technical side, one sees in Figure 6 that the GW phase shift from the data has been cut off in this example at about 25 Hz. The reason is simply that $\Delta\phi$ drops so fast with increasing f that it poses numerical challenges in resolving how the system asymptotes to the circular limit (gray dashed line) when starting from highly eccentric initial conditions. We did several checks with very fine-tuned systems to ensure that indeed we approach the circular limit $\propto f^{-13/3}$. From this, we conclude that the largest chance of seeing the GW phase shift is clearly when the system is close to its initial GW frequency, as $\Delta\phi$ quickly fades away with increasing f. This is further discussed below.

4.6. Maximum GW Phase Shift

The eccentricity for which the GW phase shift will have its peak value, i.e., where $\Delta\phi(e_m) = \max(\Delta\phi(e))$, can be estimated by deriving the eccentricity that maximizes the function $F(e)$ from Equation (27). From this, we find

$$e_m = \sqrt{\frac{2(\sqrt{391681} - 115)}{1213}} \approx 0.92. \tag{34}$$

Note that this value is slightly lower than the one we find using our full $\mathcal{PN}$ N-body simulations shown in Figure 4, which is closer to $\sim$0.95. This is partly due to our approximations such as the merger time in the eccentric limit that will, as the eccentricity decreases, end up by a factor of 768/425 larger than the true t_c when e approaches 0. These differences are not of any concern here (and could be avoided if one uses fitting functions such as the one presented in L. Zwick et al. 2020); our main result is that $\Delta\phi(e)$ has a unique form given by Equation (27) with a peak ($F(e_m) \approx 0.5$) that surprisingly is located at a universal value for the eccentricity ($e_m \sim 0.95$) regardless of the BH masses and orbital length scales. Therefore, although the source spends a significant amount of time in its eccentric state right after assembly, the maximum $\Delta\phi$ is not reached until $e \sim 0.95$. The GW phase shift, relative to the maximum value, does fall off relatively quickly when the eccentricity decreases toward merger. This is naturally given by Equation (27), which scaled to its maximum value is

$$\frac{\Delta\phi(e)}{\Delta\phi(e_m)} = \frac{F(e)}{F(e_m)} \approx 2e^{78/19}(1 - e^2)^{1/2}g(e)^{13/2}. \tag{35}$$

For example, when the source has decreased to $e \approx 0.5$, $\Delta\phi(e = 0.5)/\Delta\phi(e_m) \approx 10^{-1}$ and $\approx 10^{-2}$ at $e \approx 0.3$, which implies that, for both current and future detectors, the GW phase shift is only expected to have a significant value when the inspiraling BBH still is in its eccentric stage with $e \gtrsim 0.5$. The above relation is further shown in Figure 5. Further discussions of SNR-calculations of eccentric binaries including RDL and tidal effects are reserved for a future study, but a "rule-of-thumb" is that a LIGO-like detector can resolve GW phase shifts of the order 1 radian ×8/SNR (e.g., Y. Meiron et al. 2017), which offers an extremely promising future for GW phase shift detections from eccentric BBHs observed by 3G GW detectors, where SNR of the order $\sim$100–1000 is expected for a significant fraction of the sources.

4.7. Peak Frequency at Maximum

A relevant question relates to what the GW peak frequency is when the BBH reaches its maximum GW phase shift, denoted here by f_m, and how this is related to the initial GW peak frequency, f_0. To see this, we first use Equation (25) and rewrite it in terms of pericenter distance

$$r_p(e)/r_0 \approx 2e^{12/19}(1 + e)^{-1}g(e)g(1)^{-1}. \tag{36}$$

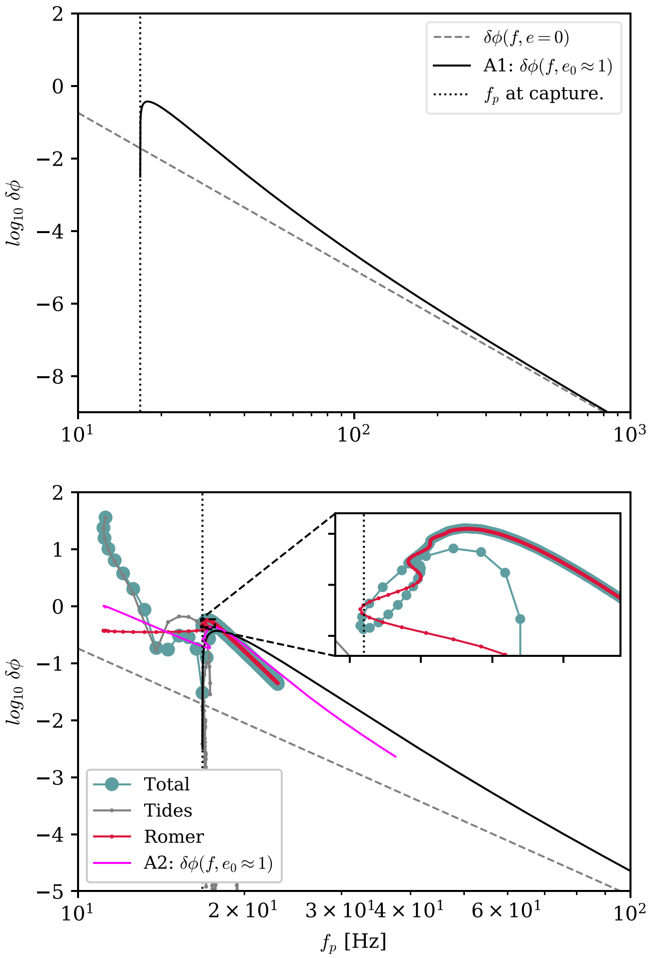

Figure 6. GW phase shift and GW peak frequency. The figures show the GW phase shift, $\delta\phi$, as a function of GW peak frequency, f_p, for the $[5M_\odot,\ 5M_\odot] + 100M_\odot$ setup from Figure 1 and Figure 4. The lines corresponding to $\delta\phi(f, e = 0)$, A1, $\delta\phi(f, e_0 \approx 1)$; and A2, $\delta\phi(f, e_0 \approx 1)$, show the analytical approximate solutions from Equation (28), Equation (33), and Equation (30), respectively. Note that Equation (33) is the only one that can be written entirely as a function of f. Top: Evolution of $\delta\phi$ from initial capture frequency f_0 (vertical dotted line) to where the eccentric approximate solution $(\propto f^{-13/3}(1 + (f_0/f))^7(1 - (f_0/f))^{1/2})$ asymptotes to the classical circular solution $(\propto f^{-13/3})$. As described in Section 4.5, the eccentric evolution rises from its asymptotic scaling $f^{-13/3}$ to a peak that is generally >10 times larger than what is found in the circular case (see Equation (32)). Bottom: Zoom in on the evolution of $\delta\phi$ around the initial GW peak frequency, f_0, with the inclusion of the data from the system shown in Figure 1. The slightly more accurate solution from Equation (30) is also included and plotted using the geometric estimated eccentricity from the data (see Section 3.1). In general, it is clear that $\delta\phi$ quickly decreases with increasing f, which adds to our conclusion from Section 4.7 that the largest GW phase shift will happen at GW frequencies around the initial frequency, f_0.

This now leads to the following expression for the ratio between the initial GW peak frequency, f_0 $(e_0 = 1)$, and the GW peak frequency leading to maximum $\Delta\phi$, f_m $(e = e_m)$

$$\frac{f_m}{f_0} \approx \left(\frac{2e_m^{12/19}}{1+e}\frac{g(e_m)}{g(1)}\right)^{-3/2} \approx 1 \quad (e_m \approx 0.95). \tag{37}$$

From this, we conclude that $f_m \sim f_0$, which means that the GW peak frequency the inspiraling BBH will have, when $\Delta\phi$ is at its maximum, will be very close to the GW peak frequency it had at formation, f_0. This leads to the conclusions we also had above, namely, that, if a BBH has to be observable near its maximum GW phase shift, the BBH has to form with an initial GW peak frequency in the observable band, or at least very close to.

4.8. Dynamical Constraints

One question remains, namely, how large can the GW phase shift $\Delta\phi$ theoretically get if we impose dynamical constraints on the input parameters? From Equation (26), we see a relatively strong dependence on the initial pericenter distance r_0, which could indicate that the GW phase shift can get extremely large, if we just allow for a large enough value of r_0. However, r_0 cannot take any value. The reason is simply that r_0, and the corresponding GW radiation emitted over one passage at this distance, is linked to the corresponding value of a_0, which has to be within the BBH Hill sphere, imposed by the perturber, R_H. To see these connections, we first note that, as the BBH consisting of m_1, m_2 essentially “forms” through a GW radiation assembly, then after the first pericenter passage, the BBH orbital energy,

$$E_0 = \frac{Gm_1m_2}{2a_0}, \tag{38}$$

will approximately equal the energy radiated over the first passage

$$\Delta E_0 \approx \frac{85\pi G^{7/2}}{12\sqrt{2}\,c^5}\frac{m_1^2m_2^2\sqrt{m_{12}}}{r_0^{7/2}}. \tag{39}$$

By now, equating E_0 and ΔE_0, we can express the initial SMA a_0 that follows from the first passage at pericenter r_0 as

$$a_0 \approx \frac{6\sqrt{2}}{85\pi}\frac{c^5}{G^{5/2}}\frac{r_0^{7/2}}{m_1m_2m_{12}^{1/2}}. \tag{40}$$

For the BBH to evolve after this first passage without being torn apart by the tidal forces of the third object with mass m_3 at distance R, its SMA a_0 has to be less than the Hill sphere given by Equation (1) by a factor β, such that $a_0 \lesssim \beta R_H$. In this setup, the maximum value for a_0 will therefore be $\sim\beta R_H$, which allow us to solve for the corresponding maximum r_0 using Equation (40), from which we find

$$r_H \approx \left(\frac{85\pi}{6\sqrt{2}}\frac{G^{5/2}}{c^5}\frac{\beta R m_1m_2m_{12}^{5/6}}{m_3^{1/3}}\right)^{2/7}. \tag{41}$$

Here, the subscript H refers to that this initial pericenter distance will result in a BBH with initial SMA a_0 that is constrained by the Hill sphere, R_H. Note that a few standard approximations are introduced in the estimation for the Hill sphere, and the value for r_H is therefore only approximate; however, it should carry the relevant scalings of the problem. The maximum GW phase shift in our setup can now be found be substituting r_0 in Equation (26) with r_H from Equation (41), after which we find

$$\begin{aligned}\Delta\phi_H(e) \;\approx\;& \frac{288\beta^{13/7}}{g(1)^{13/2}}\left(\frac{\pi^{13}}{6^{13}680}\frac{G}{c^2}\right)^{1/7}\\ &\times\left(\frac{m_3}{R}\right)^{1/7}\left(\frac{m_3 m_3}{m_1 m_2}\right)^{1/7}\left(\frac{m_{12}}{m_3}\right)^{1/21}F(e)\\ &\approx 1\times\left(\frac{\beta}{1.0}\right)^{13/7}\\ &\times\left(\frac{m_3\,/\,M_\odot}{R\,/\,AU}\right)^{1/7}\left(\frac{m_3 m_3}{m_1 m_2}\right)^{1/7}\left(\frac{m_{12}}{m_3}\right)^{1/21}F(e).\end{aligned} \tag{42}$$

We first note that the normalization is somewhat encouraging, although $\beta < 1$ (likely ~0.1–0.5 depending on the orbital parameters and objects; e.g., B. Rom et al. 2024). Furthermore, it is interesting that it does not depend strongly on neither the BH masses m nor the orbital distance R, due to the corresponding extremely low power-factors of $1/21$ and $1/7$, respectively. A maximum of $\lesssim 1$ radian for eccentric sources therefore seems like a universal upper limit according to our theoretical models, and for the setups we here consider.

However, as discussed in Section 2.5, the tidal influence from the BH3 perturber during the first few cycles of the BBH right after GW assembly can greatly affect the initial orbital conditions, which easily can bring the BBH into a regime that leads to an orbital evolution that exceeds the upper limit of $\Delta\phi$ derived above. Furthermore, if the system is chaotic, such as the example shown in Figure 8, the BBH can be brought relatively close to the remaining BH3 at merger, which would lead to a further significant increase $\propto R^{-2}$, where R is here the distance between the BBH and BH3 at merger. Another point is that our considered Hill sphere estimate only applies to interactions that are near coplanar with the orbit around the perturber, as the tidal forces that give rise to what is defined as the Hill sphere change with the orbital orientation of the binary relative to the orbital plane around the perturber. This is clear from considering the tidal tensor, which, e.g., gives rise to the well-known tidal compression in tidal disruption events that are opposite to the tidal expansion in the plane (e.g., B. Carter & J. P. Luminet 1982). To conclude, the tidal influence from the perturber and possibly chaotic evolution of the triple system can result in systems with a $\Delta\phi$ that greatly exceeds our derived limit above, which hints that observing GW phase shifts are possible under the right (observer) conditions.

To further illustrate the promising future of GW phase shift sources, we conclude this study by considering two astrophysical examples. The first being the GW capture and merger of two BHs in an AGN migration trap around an SMBH, where the second example shows results from a chaotic 3-body interaction taking place inside a GC.

5. Astrophysical Examples

The formation and properties of GW inspirals with promising GW phase shifts can be rather chaotic, at least when it comes to the normalization of the GW phase shift, as this strongly depends on the initial conditions and the following tidal couplings to the inspiraling BBH during the first few orbits. We will quantify the distribution of GW phase shifts from different BBH merger channels using statistical methods in upcoming papers, but here, we conclude this paper by presenting two astrophysically relevant cases that are known, at least theoretically, to be able to create eccentric BBH mergers with a perturber nearby.

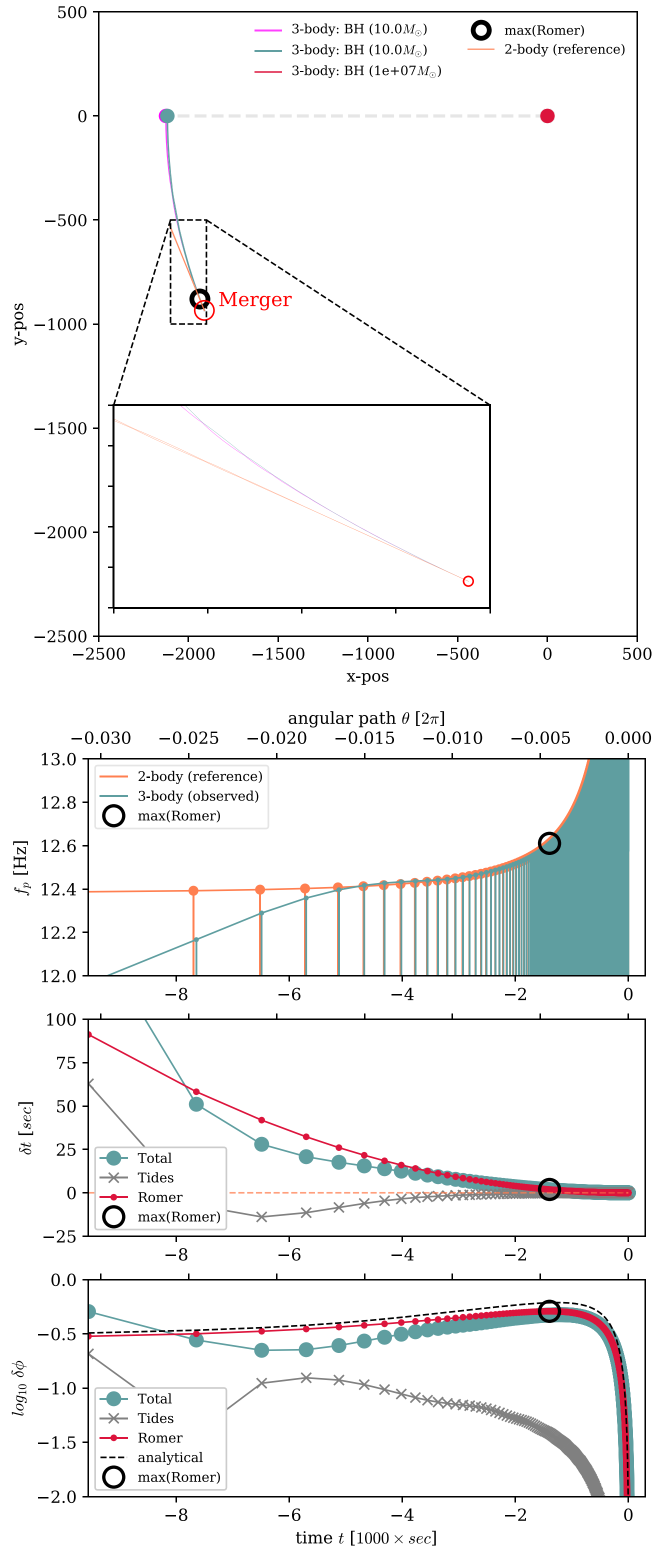

Figure 7. GW merger in an AGN migration trap. Observable differences between the 3-body-perturbed binary ($m_1 = m_2 = 10M_\odot$) orbiting a central SMBH ($m_3 = 10^7 M_\odot$) at a distance of 50 Schwarzschild radii, and the 2-body-reference binary, for the setup shown in the top panel and further described in Section 5.1.

5.1. GW Merger in an AGN Migration Trap

BBHs captured or formed in AGN disks will migrate through the disk toward the central SMBH (e.g., H. Tagawa et al. 2020). Along their way, they might undergo pairings and subsequent

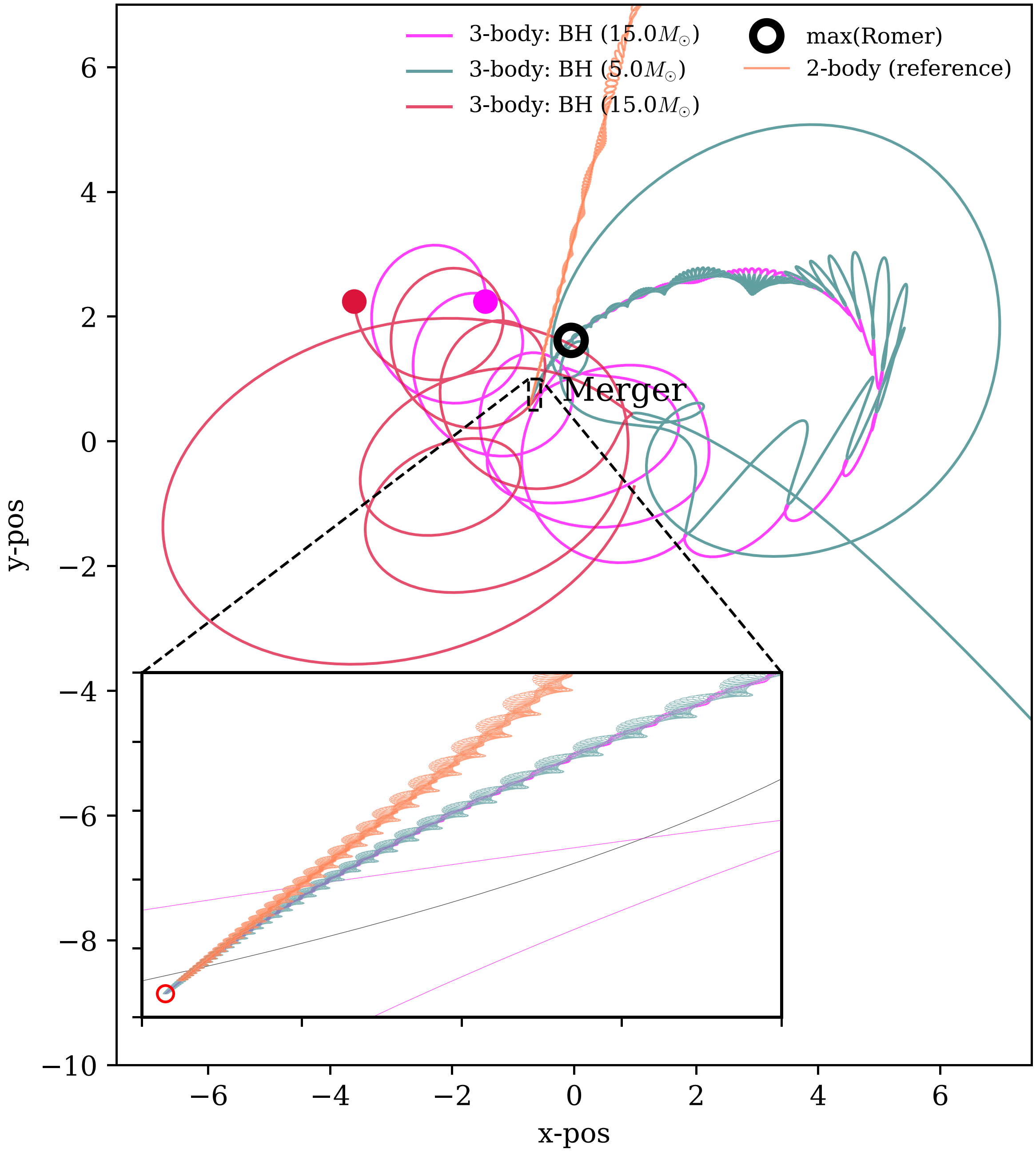

Figure 8. Chaotic 3-body scattering merger. Formation of an eccentric GW source during an interaction between a $(15M_\odot, 15M_\odot)$ BBH (red and pink) interacting with an incoming $5M_\odot$ BH (blue). As seen, the final merger is between one of the $15M_\odot$ BHs (pink) and the incoming $5M_\odot$ BH (blue). During the GW inspiral, the GW-form seen by a distant observer will be perturbed by the presence of the third bound object (red). This perturbation can be used to probe not only the existence of the third object, and thereby the underlying formation mechanism, but also the masses and orbits of the full 3-body system as in the case of binary pulsars. We quantify the perturbations by comparing the "2-body-reference" binary (orange) with the "3-body-perturbed" binary, as further explained in Section 3 and 5.2. Corresponding time- and GW phase shift results are shown in Figure 10. Three-dimensional stereographic images of this scattering is shown in Figure 9.

few-body interactions that very likely lead to mergers (e.g., J. Samsing et al. 2022). Depending on the AGN disk profile and properties, there could be so-called AGN trap regions where the migration forces switch sign giving rise to regions where BHs pile up (e.g., J. M. Bellovary et al. 2016). These are known as "migration traps" and could naturally facilitate a pit for bringing BHs to merger. As described in, e.g., J. M. Bellovary et al. (2016), migration traps can be found at distances as close as $\sim 50 \times \mathscr{R}_3$ from the SMBH, where $\mathscr{R}_3$ denotes the Schwarzschild radius of the SMBH (BH3). The location and even existence of these AGN migration traps are still under debate from a theoretical perspective, but GW observations can help constraining these models, as we show here.

We consider a BBH ($m_1 = m_2 = 10M_\odot$) undergoing a GW assembly and subsequent inspiral around an SMBH ($m_3 = 10^7 M_\odot$), at a distance $R = 50\mathscr{R}_3$. The evolution and resulting GW phase shift for this system are shown in Figure 7. As seen, the BBH has an initial GW peak frequency near the LVK band and a corresponding maximum GW phase shift approaching 1 radian. Such BBH mergers forming in AGN traps therefore have the potential to be observed even with current detectors, and certainly with future 3G detectors, which

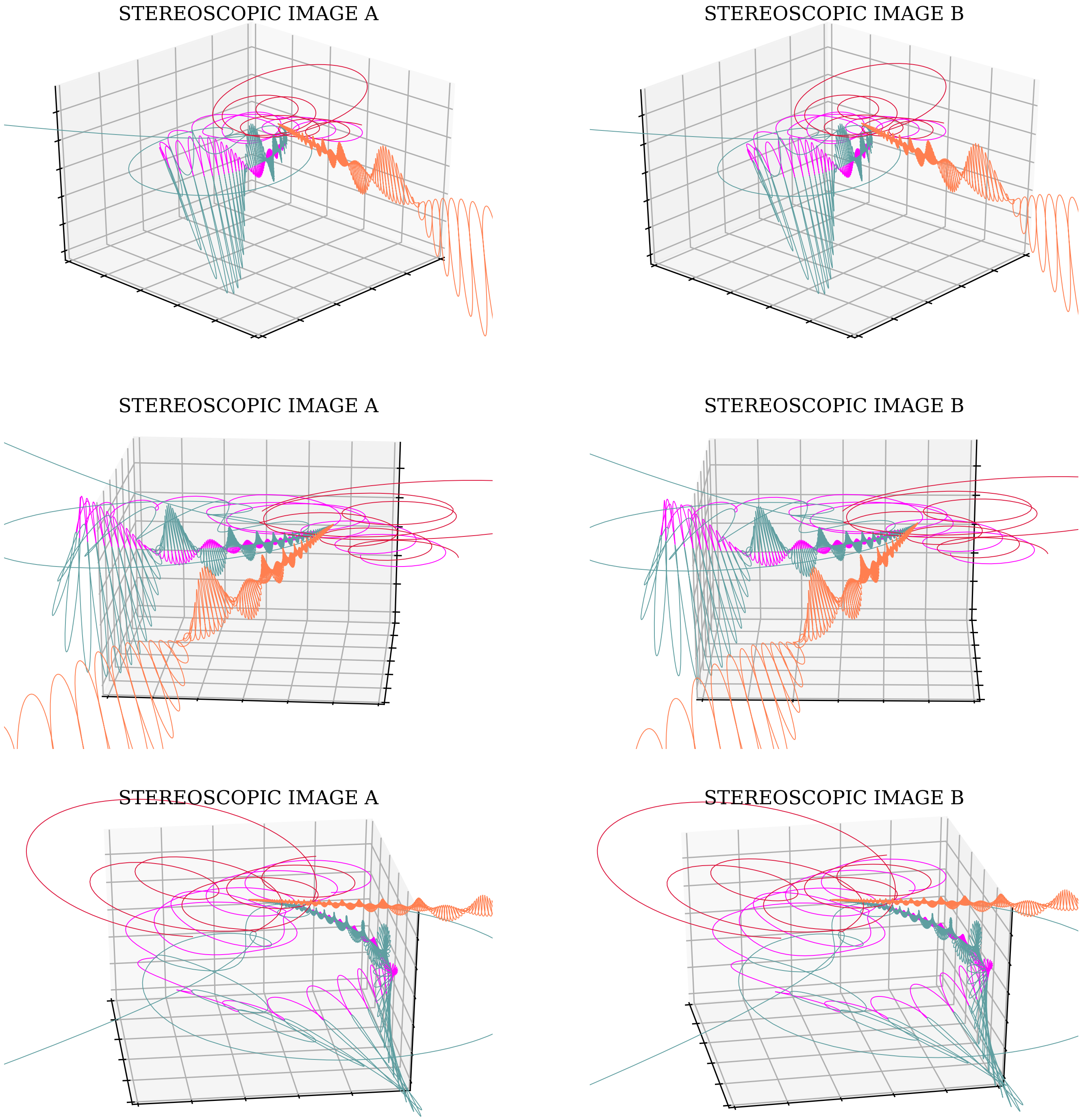

Figure 9. Stereoscopic three-dimensional images. The three horizontal panels each show three-dimensional plots of the chaotic 3-body scattering from Figure 8, to provide a three-dimensional understanding for how and where the 2-body-reference binary is in relation to the 3-body-perturbed binary. To see and experience the three-dimensional effect, one has to visually overlap "STEREOSCOPIC IMAGE A" with "STEREOSCOPIC IMAGE B" using a cross-eyed view. This is how you do it: Look normally at a point right between image "A" and "B." Now, take your finger up in front of your eyes along your line of sight. While keeping your focus on the point right between image "A" and "B," move your finger back and forth until the two images you see of your finger visually are "on top" and in "the middle" of each image "A" and "B." Now, shift your focus to your finger. Without shifting focus, remove your finger, and make a slight adjustment to now see image "A" and "B" overlap to form one three-dimensional picture popping out of the screen/paper. With a bit of practice, you will be able to quickly see these stereoscopic images while your fingers are safely placed in your pocket.

encourages more detailed work on such GW phase shift effects in BBHs forming dynamically in AGN disk environments.

5.2. *Chaotic 3-body Scattering Merger*

One of the most reliable mechanisms for producing BBH mergers dynamically is through 3-body scatterings in dense stellar systems, in particular GCs (C. L. Rodriguez et al. 2018b; J. Samsing 2018; J. Samsing et al. 2018a; M. Zevin et al. 2019; F. Antonini & M. Gieles 2020). In this scenario, the heavier BHs in the cluster sink to the center, also known as mass segregation, to form a small subcluster of black holes with relatively high density. Here, the BHs pair up to form soft and

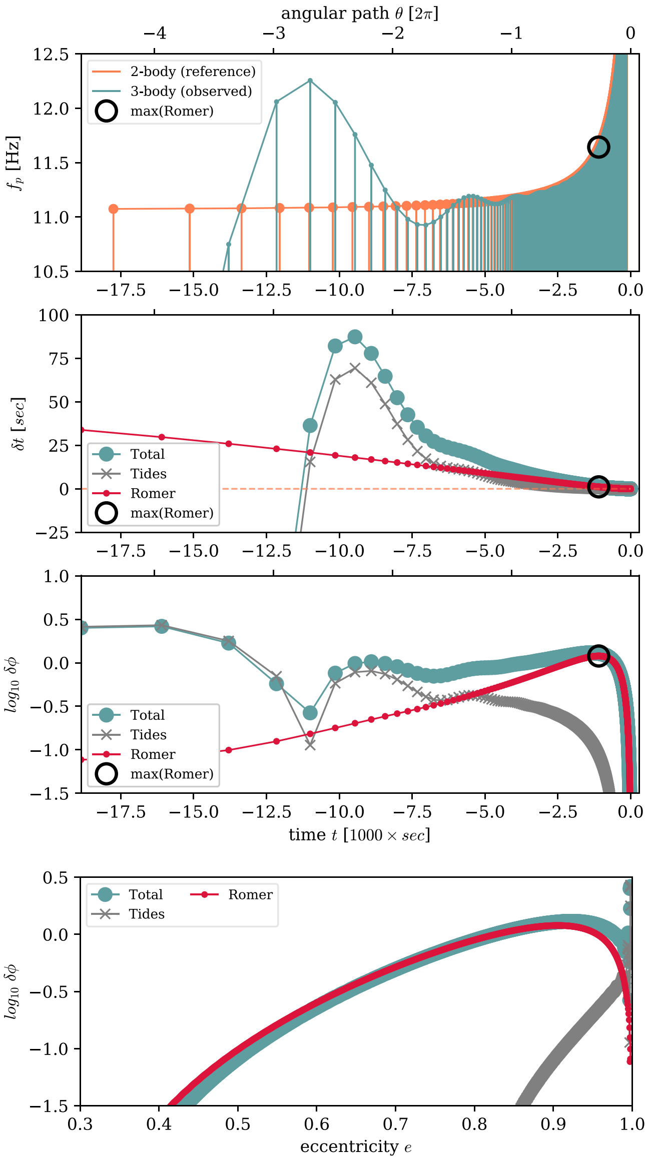

Figure 10. Chaotic 3-body scattering merger. Observable differences between the 3-body-perturbed binary and the 2-body-reference binary shown in Figure 8, and discussed in Section 2.2. We see how the unique features we derived in Section 4, such as a maximum in the GW phase shift from Rømer delay, are still present here in the case of a chaotic interaction. Larger differences between the outer-orbit being eccentric compared to circular, will be explored in upcoming papers.

wide binaries, which subsequently undergo interactions with the single BH population, also known as 3-body interactions. These interactions not only stabilize the cluster through dynamical heating but also bring the BBHs close enough together for them to occasionally undergo a GW merger either inside or outside of the cluster (e.g., J. Samsing & D. J. D'Orazio 2018). In J. Samsing (2018), it was in particular shown that about 10% of all BBH mergers formed dynamically in GCs will merge inside the cluster while being bound to the single BH that triggered the merger, often referred to as a chaotic "3-body merger."

Figure 8 shows an example of the formation of such a 3-body merger, where the three panels in Figure 9 show the same example from three different observer positions in *Stereoscopic Vision* (see caption for more details). The initial binary is composed of two BHs each with a mass of $15M_{\odot}$ at a separation of $a_0 = 0.01$ au, where the incoming BH has a mass of $5M_{\odot}$. On the figures are also overplotted a 2-body-reference binary, as we did in the more idealized cases shown above. Figure 10 shows the corresponding differences between the 3-body-perturbed binary and our 2-body-reference binary. As seen for this particular system, the maximum GW phase shift is close to ∼1 radian. Note also, in Figure 8, that the BBH as it spirals in actually evolves close to one full orbit around the bound single BH. This gives rise to additional modulation effects than the one we worked out in Section 4 above, but they are of course naturally included in our numerical results shown here. However, the main characteristics of this chaotically assembled eccentric GW phase shift source are the same as in our considered idealized analytical case; one sees a clear peak in the GW phase shift around $e \sim 0.95$, and a corresponding rapid decrease as a function of decreasing eccentricity e. An effect that also remains to be quantified is the effect from the outer orbit to be eccentric, as this effectively will give rise to a varying curvature or effective radius, R, along the orbit. It can happen here, e.g., that the BBH inspiral passes through the pericenter of the outer orbit, which could give rise to an additional increase in the GW phase shift off centered from the maximum $e \sim 0.95$ that exists in the circular outer-orbit case. Other effects can be gravitational redshift, which could dominate over the RDL depending on the outer orbit eccentricity and position of the observer. We will quantify these effects in upcoming papers, and link the overall GW phase shift distribution at different GW frequencies to the specific underlying dynamical channels and properties of the environment.

6. Conclusions

In this paper, we have quantified the GW phase shift appearing in the GW-form of eccentric inspirals evolving near a perturber, as a result of including the time changing Doppler shift giving rise to a RDL, and the tidal influence of the perturber. By accurately measuring the time-dependent GW phase shift, one can in principle infer the mass and orbits of the entire 3-body system, as in the case of binary pulsars, which offer unique possibilities for learning about the formation environment and mechanisms of dynamically formed BBH mergers (see also Y. Meiron et al. 2017). With upcoming GW detectors such as ET and CE that are expected to achieve SNRs of 100–1000 for BBH mergers, such GW phase shift measurements will become one of the most powerful ways of probing the origin of individual GW sources using GWs alone.

Previous work has mainly focused on circular binaries on circular orbits near heavy perturbers; however, we point out that the most likely case is that the majority of sources with nearby perturbers must have been eccentric in the past, while some might even be at the time of observation. The question of how the GW phase shift changes as a function of time, eccentricity, and GW frequency is therefore crucial to understand for making realistic couplings between theory and observations.

For our work, we have developed a new numerical approach that is based on a novel technique, where we construct an unperturbed reference binary by evolving the $\mathcal{PN}$ equations backwards from a point near merger. The properties of this 2-body-reference binary are compared to the 3-body-perturbed binary, from which we can quantify the tiniest variations in, e.g., the observed GW signal emitted by the observed, 3-body-perturbed binary. In our framework so far, we only include dynamical perturbations, and the contributions from RDL, as these effects were argued in Y. Meiron et al. (2017) to likely be dominating for most astrophysical systems. We do however plan on including more relativistic effects in upcoming versions.

We further present an analytical solution, which is an extension to the well-known GW phase shift relations in the circular case, but now with the inclusion of eccentricity, e. This gives, in particular, rise to a new and unique relation between maximum GW phase shift, $\Delta\phi$, and eccentricity, e. Including eccentricity is crucial, as the most likely GW phase shift candidates will have formed dynamically, or at least in a dynamical environment, which means their initial eccentricity at assembly will be nonzero.

Besides a few idealized examples of an eccentric, merging binary on a circular orbit around a central BH, we have also considered GW phase shifts from chaotic 3-body scatterings, which will occur frequently in GCs and other dense stellar systems. The chaotic nature of this channel and corresponding GW phase shifts call for a more statistical approach to make predictions for different systems, which we plan on doing in upcoming papers.

From this first study of the observable perturbed GW signal from an eccentric BBH inspiraling on an orbit around a third perturbing BH, we identify the following main results:

1. The RDL, which is linked to the nonrelativistic Doppler effect, leads to a GW phase shift $\Delta\phi$ of the eccentric BBH orbiting the third BH, which we find evolves in a unique way as a function of eccentricity, e, as $\Delta\phi \propto 2e^{78/19}(1-e^2)^{1/2}g(e)^{13/2}$ (see Equation (26)). This form does not depend on either the BH masses or any length scales; it only depends on eccentricity, which implies that the maximum GW phase shift, and how it evolves near its maximum value, can be deduced from this simple equation. For example, one can see that the GW phase shift is maximized when the BBH reaches an eccentricity of $e \sim 0.95$, and already reduced by a factor of 10 when $e \sim 0.5$ (see Section 4.6). This strongly suggests that, for GW phase shifts to be observable for dynamically assembled sources, we need to catch them in their eccentric phase. Note here that these are general statements, where details will depend trivially on the position of the observer.
2. The tidal influence from the third BH can give rise to significant changes to the orbital parameters of the inspiraling BBH right after assembly, which first results in clear wavelike perturbations to the GW peak frequency signal (Figure 4). The wave period is directly related to the $1\mathcal{PN} + 2\mathcal{PN}$-precession period of the inspiraling BBH, which, if observed, will put tighter constrains on the system. The tidal coupling also affects the later stages of the inspiraling BBH, as the maximum GW phase shift effectively depends on the initial conditions, which sets the merger time and thereby essentially how much the binary COM motion will differ from a standard reference binary evolving on a straight line (Section 4.2). As a result, we argue and find that, when tidal interactions are taken into account, the BBH orbital parameters can in some cases be changed to result in much larger GW phase shifts than the analytical models predict.
3. The GW peak frequency of the BBH when it reaches its maximum GW phase shift is very close to the GW peak frequency at formation (Section 37), i.e., when $f_m \sim f_0$. This implies that sources that are expected to give rise to the largest observable GW phase shifts (observable in terms of peak frequency) also will have to form with f_0 near the observable band. Many channels involving 3-body systems are expected to give rise to at least a fraction of sources that form with f_0 directly in the observable band (e.g., J. Samsing et al. 2022). Eccentric sources with GW phase shifts are therefore expected to exist; the question is if the third object is close enough for the shift to be large enough to be observable. That depends not only on the chaotic nature of the systems but also more broadly on the velocity dispersion of the underlying environment, as this sets the characteristic size of the 3-body system and thereby roughly the magnitude of the GW phase shift.
4. The GW phase shift as a function of GW peak frequency, f_p, is of direct interest in terms of observations, and has been shown in the circular case to scale $\propto f^{-13/3}$. However, when the BBH is evolving with a nonzero eccentricity, this simple relation does not hold; instead, we find an approximate solution that takes the form $\propto f^{-13/3} \times (1 + (f_0/f))^7 (1 - (f_0/f))^{1/2}$. This implies that the GW phase shift actually increases faster toward lower GW peak frequencies compared to the circular case, with a peak that can be $\sim$30 times larger near the binary formation frequency compared to the case of circular binaries. This we confirmed with our simulations shown in Figure 6, and as further discussed in Section 4.5.

With the theory and new numerical framework presented in this paper, we will in upcoming papers study the outcomes from a large ensemble of few-body scatterings taking place in astrophysical systems from GCs to AGN disks, and statistically quantify the observable possibilities in relation to LISA, DECIGO, 3G detectors, and LVK.

Acknowledgments

It is a pleasure to thank Martin Pessah, Zihan Zhou, and Yan Yu for enlightening discussions. The authors also thank the Research Center for the Early Universe (RESCEU) at Tokyo University where part of this work was completed. J.S., K.H., and L.Z. are supported by the Villum Fonden grant No. 29466, and by the ERC Starting grant No. 101043143—BlackHoleMergs. B.L. gratefully acknowledges support from the European Union's Horizon 2021 research and innovation program under the Marie Sklodowska-Curie grant agreement No. 101065374. The Center of Gravity is a Center of Excellence funded by the Danish National Research Foundation under grant No. 184.

Appendix

Below, we show a few specific cases to illustrate the importance of using numerical prescriptions, such as the $\mathcal{PN}$ framework we have introduced that mixes forward and backward evolutions (perturbed and reference binary, respectively), for solving the binary and single problem with corresponding GW phase shifts. We highlight below in particular the sensitivity to the initial conditions, and the importance of including the $1\mathcal{PN}$, $2\mathcal{PN}$ energy conserving precession terms.

A.1. Sensitivity to Initial Conditions and Tides

The 3-body systems that are expected to give rise to the largest GW phase shifts are generally also the ones where the binary is assembled with an SMA about the size of the Hill sphere (see Section 4.6 and Figure 2). The reason is simply that the less compact the binary is, the larger the merger time generally will be, and the more the binary COM trajectory from assembly to merger will differ from a straight line. The most relevant 3-body systems are therefore the ones where the initial BBH is most easily perturbed by tidal interactions during its early evolutionary stages of the inspiral phase. We here show the sensitivity to the initial conditions when the BBH is assembled near the Hill sphere, and how this impacts the evolution and corresponding GW phase shift.

Figure 11 shows essentially the same setup as the one studied in Section 2.2, but with minor changes to the initial SMA. As seen, in the left panel, the tidal interaction between the binary and the third BH leads to an irregular inspiral at early times, after which the tidal forces perturb the BBH orbit into a combination of values that lead to a fast merger. The short merger time implies a relatively high GW peak frequency, as seen to be around 30 Hz at formation, but also a corresponding small GW phase shift as seen in the bottom panel and expected from, e.g., Equation (26), which shows $\Delta\phi \propto f_0^{-13/3}$. In the right panel of Figure 11, the tides lead instead to a more long-term and gradual inspiral, which evolves over the entire outer orbit. The final assembly at inspiral takes place with a GW peak frequency of around 20 Hz, which therefore leads to a GW phase shift that is 1–2 orders of magnitude larger than the evolution shown in the left panel. This example clearly illustrates the chaotic nature of the tidal and $\mathcal{PN}$ couplings at early times, and how they affect the late time evolution and corresponding maximum GW phase shift. The effect from tides therefore brings both opportunities and difficulties that we will explore in upcoming papers.

A.2. Importance of the $1\mathcal{PN}$, $2\mathcal{PN}$ Precession Terms:

The dissipative $2.5\mathcal{PN}$ term is the one that leads to the gradual inspiral and eventual merger of the BBH. However, as we have argued in the above Appendix A.1 and in Section 2.2, the BBHs that are most likely to give rise to measurable GW shifts are also the ones that are most likely to be in tidal contact with the third BH during the early stages of their inspiral phase. This tidal influence on the binary was, I. Romero-Shaw et al. (2023) argued, using a simple analytical toy-model, to lead to a gradual build up in the GW phase shift, which could be used for probing the presence of the third BH; however, the model that was developed for this did not include the conservative precession terms $1\mathcal{PN}$, $2\mathcal{PN}$. We here show the crucial importance of including these terms, as we also argued in Section 2.5.

We now consider Figure 12, which shows in the left panel the same example as we considered in Section 2.2, and in the right panel results from similar initial conditions, but without the inclusion of the conservative $1\mathcal{PN}$, $2\mathcal{PN}$ terms. As seen in the right panel, when the BBH by construction is not able to precess, the tidal force on the BBH from the third BH is simply gradually building up to result in a predictable and smooth evolution of the GW phase shift, that, as a result, is driven to a huge value at its peak. This is clearly an unphysical result, which illustrates the importance of a correct dynamical implementation for evolving such systems. The conservative $1\mathcal{PN}$, $2\mathcal{PN}$ terms have also been shown to play a major role in the evolution of hierarchical 3-body systems (e.g., S. Naoz 2016).

The fact that the few-body evolution and corresponding GW phase shift depend so strongly on how the binary tidally couples to the third object also brings some concerns to our model, as this also is not fully accurate mainly due to approximations in the $\mathcal{PN}$ formalism. However, while more accurate models can be adapted, we do believe that we have been able to resolve the main effects of the problem using our model. Further effects will be explored in upcoming papers, such as outer orbit eccentricity and binary tilt, as well as black hole spins; effects that all will result in their own GW phase shift contribution.

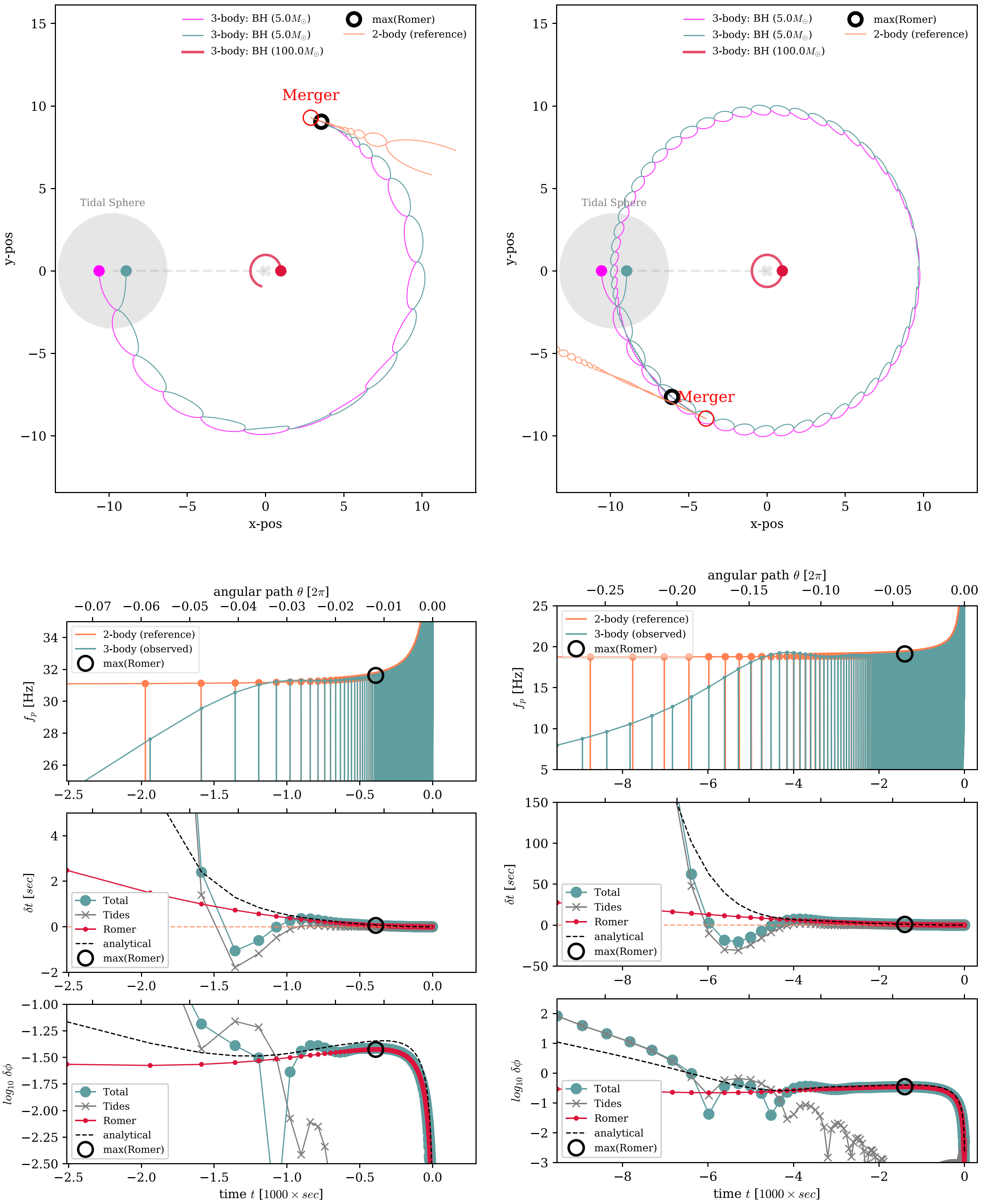

Figure 11. Sensitivity to initial conditions and tides: Examples similar to the one introduced in Figure 1, differing only slightly in the initial SMA a_0 as seen in the figure. The significant differences in both orbital evolution and corresponding GW phase shifts between the left and right panel are due to tidal couplings between the binary and the central BH early times in their inspiral. This coupling depends not only on the binary SMA and eccentricity, a, e, but also on the orbital orientation and binary phase. Numerical studies, as the one we show in this paper, are therefore crucial in making accurate predictions for how to link theory to observations.

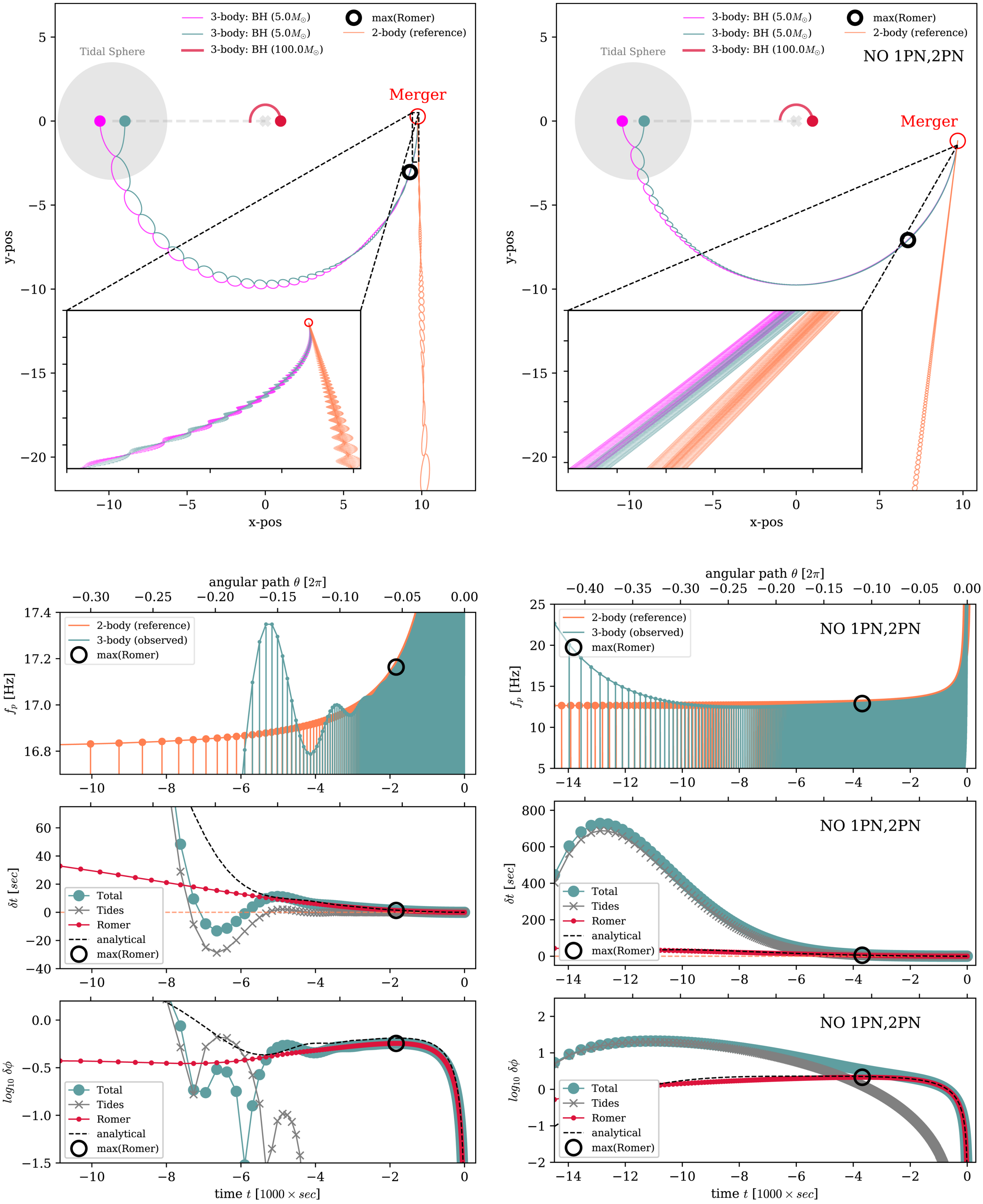

Figure 12. Importance of the $1\mathcal{PN}$, $2\mathcal{PN}$ precession terms: Left panel shows our considered example from Figure 1, where the right panel shows a similar system for comparison, but without the inclusion of the $1\mathcal{PN}$, $2\mathcal{PN}$ precession terms in the EOM ("NO 1PN, 2PN"). As seen, when $\mathcal{PN}$ precession is not included, tides from the central BH3 can without any problem gradually build up to result in large time- and GW phase shifts. This is incorrect, and serves therefore as a clear illustration to why the conservative $1\mathcal{PN}$, $2\mathcal{PN}$ terms are crucial.

ORCID iDs

Johan Samsing https://orcid.org/0000-0003-0607-8741
Daniel J. D'Orazio https://orcid.org/0000-0002-1271-6247
Bin Liu https://orcid.org/0000-0002-0643-8295

References

Abbott, B. P., Abbott, R., Abbott, T. D., et al. 2019a, ApJL, 882, L24
Abbott, B. P., Abbott, R., Abbott, T. D., et al. 2019b, ApJ, 883, 149
Abbott, R., Abbott, T. D., Abraham, S., et al. 2020, PhRvL, 125, 101102
Abbott, R., Abe, H., Acernese, F., et al. 2023, ApJS, 267, 29
Amaro-Seoane, P., Audley, H., Babak, S., et al. 2017, arXiv:1702.00786
Antognini, J. M. O., & Thompson, T. A. 2016, MNRAS, 456, 4219
Antonini, F., Chatterjee, S., Rodriguez, C. L., et al. 2016, ApJ, 816, 65
Antonini, F., & Gieles, M. 2020, MNRAS, 492, 2936
Antonini, F., & Rasio, F. A. 2016, ApJ, 831, 187
Arca Sedda, M., Mapelli, M., Spera, M., Benacquista, M., & Giacobbo, N. 2020, ApJ, 894, 133
Askar, A., Szkudlarek, M., Gondek-Rosińska, D., Giersz, M., & Bulik, T. 2017, MNRAS, 464, L36
Atallah, D., Trani, A. A., Kremer, K., et al. 2023, MNRAS, 523, 4227
Bae, Y.-B., Kim, C., & Lee, H. M. 2014, MNRAS, 440, 2714
Banerjee, S., Baumgardt, H., & Kroupa, P. 2010, MNRAS, 402, 371
Barausse, E., Cardoso, V., & Pani, P. 2014, PhRvD, 89, 104059
Bartos, I., Kocsis, B., Haiman, Z., & Márka, S. 2017, ApJ, 835, 165
Belczynski, K., Holz, D. E., Bulik, T., & O'Shaughnessy, R. 2016a, Natur, 534, 512
Belczynski, K., Repetto, S., Holz, D. E., et al. 2016b, ApJ, 819, 108
Bellovary, J. M., Mac Low, M.-M., McKernan, B., & Ford, K. E. S. 2016, ApJL, 819, L17
Bird, S., Cholis, I., Muñoz, J. B., et al. 2016, PhRvL, 116, 201301
Biscoveanu, S., Callister, T. A., Haster, C.-J., et al. 2022, ApJL, 932, L19
Blanchet, L. 2006, LRR, 9, 4
Blanchet, L. 2014, LRR, 17, 2
Bonino, A., Gamba, R., Schmidt, P., et al. 2023, PhRvD, 107, 064024
Breivik, K., Rodriguez, C. L., Larson, S. L., Kalogera, V., & Rasio, F. A. 2016, ApJL, 830, L18
Camilloni, F., Grignani, G., Harmark, T., Orselli, M., & Pica, D. 2024, MNRAS, 531, 1884
Camilloni, F., Grignani, G., Harmark, T., et al. 2023, PhRvD, 107, 084011
Carr, B., Kühnel, F., & Sandstad, M. 2016, PhRvD, 94, 083504
Carter, B., & Luminet, J. P. 1982, Natur, 296, 211
Chamberlain, K., Moore, C. J., Gerosa, D., & Yunes, N. 2019, PhRvD, 99, 024025
Chen, X., & Amaro-Seoane, P. 2017, ApJL, 842, L2
Cholis, I., Kovetz, E. D., Ali-Haïmoud, Y., et al. 2016, PhRvD, 94, 084013
Ciarfella, A., Healy, J., Lousto, C. O., & Nakano, H. 2022, PhRvD, 106, 104035
Dai, L., Li, S.-S., Zackay, B., Mao, S., & Lu, Y. 2018, PhRvD, 98, 104029
Dominik, M., Belczynski, K., Fryer, C., et al. 2012, ApJ, 759, 52
Dominik, M., Belczynski, K., Fryer, C., et al. 2013, ApJ, 779, 72
Dominik, M., Berti, E., O'Shaughnessy, R., et al. 2015, ApJ, 806, 263
D'Orazio, D. J., & Loeb, A. 2018, PhRvD, 97, 083008
D'Orazio, D. J., & Loeb, A. 2020, PhRvD, 101, 083031
D'Orazio, D. J., & Samsing, J. 2018, MNRAS, 481, 4775
Evans, M., Corsi, A., Afle, C., et al. 2023, arXiv:2306.13745
Fabj, G., & Samsing, J. 2024, MNRAS, 535, 3630
Farr, W. M., Fishbach, M., Ye, J., & Holz, D. E. 2019, ApJL, 883, L42
Fishbach, M., & Fragione, G. 2023, MNRAS, 522, 5546
Fishbach, M., Holz, D. E., & Farr, W. M. 2018, ApJL, 863, L41
Garcìa-Bellido, J., Nuño Siles, J. F., & Ruiz Morales, E. 2021, PDU, 31, 100791
Gayathri, V., Healy, J., Lange, J., et al. 2022, NatAs, 6, 344
Gültekin, K., Miller, M. C., & Hamilton, D. P. 2006, ApJ, 640, 156
Gupte, N., Ramos-Buades, A., Buonanno, A., et al. 2024, arXiv:2404.14286
Hamers, A. S., Bar-Or, B., Petrovich, C., & Antonini, F. 2018, ApJ, 865, 2
Hamers, A. S., & Samsing, J. 2019, MNRAS, 487, 5630
Hamers, A. S., & Thompson, T. A. 2019, ApJ, 883, 23
Han, W.-B., Yang, S.-C., Tagawa, H., et al. 2025, ApJL, 988, L41
Hoang, B.-M., Naoz, S., Kocsis, B., Rasio, F. A., & Dosopoulou, F. 2018, ApJ, 856, 140
Hong, J., & Lee, H. M. 2015, MNRAS, 448, 754
Hu, W.-R., & Wu, Y.-L. 2017, NSRev, 4, 685
Inayoshi, K., Tamanini, N., Caprini, C., & Haiman, Z. 2017, PhRvD, 96, 063014
Iorio, G., Mapelli, M., Costa, G., et al. 2023, MNRAS, 524, 426
Janiuk, A., Bejger, M., Charzyński, S., & Sukova, P. 2017, NewA, 51, 7
Kalogera, V. 2000, ApJ, 541, 319
Kawamura, S., Ando, M., Seto, N., et al. 2011, CQGra, 28, 094011
Kremer, K., Rodriguez, C. L., Amaro-Seoane, P., et al. 2019, PhRvD, 99, 063003
Kupi, G., Amaro-Seoane, P., & Spurzem, R. 2006, MNRAS, 371, L45
Laeuger, A., Seymour, B., Chen, Y., & Yu, H. 2024, PhRvD, 109, 064086
Lee, W. H., Ramirez-Ruiz, E., & van de Ven, G. 2010, ApJ, 720, 953
Li, G., Naoz, S., Kocsis, B., & Loeb, A. 2014, ApJ, 785, 116
Liu, B., & Lai, D. 2018, ApJ, 863, 68
Liu, B., & Lai, D. 2021, MNRAS, 502, 2049
Liu, B., Lai, D., & Wang, Y.-H. 2019a, ApJL, 883, L7
Liu, B., Lai, D., & Wang, Y.-H. 2019b, ApJ, 881, 41
Liu, S., Hu, Y.-M., Zhang, J.-d., & Mei, J. 2020, PhRvD, 101, 103027
Loeb, A. 2016, ApJL, 819, L21
Luo, J., Chen, L.-S., Duan, H.-Z., et al. 2016, CQGra, 33, 035010
Maggiore, M., Van Den Broeck, C., Bartolo, N., et al. 2020, JCAP, 2020, 050
Martinez, M. A. S., Fragione, G., Kremer, K., et al. 2020, ApJ, 903, 67
McKernan, B., Ford, K. E. S., Bellovary, J., et al. 2018, ApJ, 866, 66
Meiron, Y., Kocsis, B., & Loeb, A. 2017, ApJ, 834, 200
Murguia-Berthier, A., MacLeod, M., Ramirez-Ruiz, E., Antoni, A., & Macias, P. 2017, ApJ, 845, 173
Naoz, S. 2016, ARA&A, 54, 441
Naoz, S., Kocsis, B., Loeb, A., & Yunes, N. 2013, ApJ, 773, 187
O'Leary, R. M., Kocsis, B., & Loeb, A. 2009, MNRAS, 395, 2127
Park, D., Kim, C., Lee, H. M., Bae, Y.-B., & Belczynski, K. 2017, MNRAS, 469, 4665
Peters, P. C. 1964, PhRv, 136, 1224
Portegies Zwart, S. F., & McMillan, S. L. W. 2000, ApJ, 528, L17
Ramirez-Ruiz, E., Trenti, M., MacLeod, M., et al. 2015, ApJL, 802, L22
Randall, L., & Xianyu, Z.-Z. 2018, ApJ, 864, 134
Randall, L., & Xianyu, Z.-Z. 2019, ApJ, 878, 75
Robson, T., Cornish, N. J., Tamanini, N., & Toonen, S. 2018, PhRvD, 98, 064012
Rodriguez, C. L., Amaro-Seoane, P., Chatterjee, S., et al. 2018a, PhRvD, 98, 123005
Rodriguez, C. L., Amaro-Seoane, P., Chatterjee, S., & Rasio, F. A. 2018b, PhRvL, 120, 151101
Rodriguez, C. L., & Antonini, F. 2018, ApJ, 863, 7
Rodriguez, C. L., Chatterjee, S., & Rasio, F. A. 2016a, PhRvD, 93, 084029
Rodriguez, C. L., Haster, C.-J., Chatterjee, S., Kalogera, V., & Rasio, F. A. 2016b, ApJL, 824, L8
Rodriguez, C. L., Morscher, M., Pattabiraman, B., et al. 2015, PhRvL, 115, 051101
Rodriguez, C. L., Zevin, M., Pankow, C., Kalogera, V., & Rasio, F. A. 2016c, ApJL, 832, L2
Rom, B., Sari, R., & Lai, D. 2024, ApJ, 964, 43
Romero-Shaw, I., Lasky, P. D., & Thrane, E. 2021, ApJL, 921, L31
Romero-Shaw, I., Lasky, P. D., & Thrane, E. 2022, ApJ, 940, 171
Romero-Shaw, I., Loutrel, N., & Zevin, M. 2023, PhRvD, 107, 122001
Romero-Shaw, I. M., Kremer, K., Lasky, P. D., Thrane, E., & Samsing, J. 2021, MNRAS, 506, 2362
Samsing, J. 2018, PhRvD, 97, 103014
Samsing, J., Askar, A., & Giersz, M. 2018a, ApJ, 855, 124
Samsing, J., & D'Orazio, D. J. 2018a, MNRAS, 481, 5445
Samsing, J., D'Orazio, D. J., Kremer, K., Rodriguez, C. L., & Askar, A. 2020, PhRvD, 101, 123010
Samsing, J., Hamers, A. S., & Tyles, J. G. 2019, PhRvD, 100, 043010
Samsing, J., & Ilan, T. 2018, MNRAS, 476, 1548
Samsing, J., MacLeod, M., & Ramirez-Ruiz, E. 2014, ApJ, 784, 71
Samsing, J., MacLeod, M., & Ramirez-Ruiz, E. 2018b, ApJ, 853, 140
Samsing, J., & Ramirez-Ruiz, E. 2017, ApJL, 840, L14
Samsing, J., Bartos, I., D'Orazio, D. J., et al. 2022, Natur, 603, 237
Sasaki, M., Suyama, T., Tanaka, T., & Yokoyama, S. 2016, PhRvL, 117, 061101
Schroder, S. L., Batta, A., & Ramirez-Ruiz, E. 2018, ApJL, 862, L3
Sesana, A. 2016, PhRvL, 116, 231102
Shaikh, M. A., Varma, V., Pfeiffer, H. P., Ramos-Buades, A., & van de Meent, M. 2023, PhRvD, 108, 104007
Silsbee, K., & Tremaine, S. 2017, ApJ, 836, 39
Stephan, A. P., Naoz, S., Ghez, A. M., et al. 2016, MNRAS, 460, 3494
Stone, N. C., Metzger, B. D., & Haiman, Z. 2017, MNRAS, 464, 946
Strokov, V., Fragione, G., Wong, K. W. K., Helfer, T., & Berti, E. 2022, PhRvD, 105, 124048

Su, Y., Liu, B., & Lai, D. 2021, MNRAS, 505, 3681
Tagawa, H., Haiman, Z., & Kocsis, B. 2020, ApJ, 898, 25
Tamanini, N., Klein, A., Bonvin, C., Barausse, E., & Caprini, C. 2020, PhRvD, 101, 063002
Tanikawa, A. 2013, MNRAS, 435, 1358
The LIGO Scientific Collaboration, the Virgo Collaboration, the KAGRA Collaboration, et al. 2024, ApJ, 973, 132
Tiwari, A., Vijaykumar, A., Kapadia, S. J., Fragione, G., & Chatterjee, S. 2024, MNRAS, 527, 8586
Toubiana, A., Sberna, L., Caputo, A., et al. 2021, PhRvL, 126, 101105
Trani, A. A., Quaini, S., & Colpi, M. 2024, A&A, 683, A135
Trani, A. A., Rastello, S., Di Carlo, U. N., et al. 2022, MNRAS, 511, 1362
Trani, A. A., Spera, M., Leigh, N. W. C., & Fujii, M. S. 2019, ApJ, 885, 135
Trani, A. A., Tanikawa, A., Fujii, M. S., Leigh, N. W. C., & Kumamoto, J. 2021, MNRAS, 504, 910
Tucker, A., & Will, C. M. 2021, PhRvD, 104, 104023
van Son, L. A. C., de Mink, S. E., Callister, T., et al. 2022, ApJ, 931, 17
VanLandingham, J. H., Miller, M. C., Hamilton, D. P., & Richardson, D. C. 2016, ApJ, 828, 77
Vijaykumar, A., Tiwari, A., Kapadia, S. J., Arun, K. G., & Ajith, P. 2023, ApJ, 954, 105
Wong, K. W. K., Baibhav, V., & Berti, E. 2019, MNRAS, 488, 5665
Woosley, S. E. 2016, ApJL, 824, L10
Xuan, Z., Naoz, S., & Chen, X. 2023, PhRvD, 107, 043009
Yunes, N., Miller, M. C., & Thornburg, J. 2011, PhRvD, 83, 044030
Zackay, B., Venumadhav, T., Dai, L., Roulet, J., & Zaldarriaga, M. 2019, PhRvD, 100, 023007
Zevin, M., Bavera, S. S., Berry, C. P. L., et al. 2021a, ApJ, 910, 152
Zevin, M., Pankow, C., Rodriguez, C. L., et al. 2017, ApJ, 846, 82
Zevin, M., Romero-Shaw, I. M., Kremer, K., Thrane, E., & Lasky, P. D. 2021b, ApJL, 921, L43
Zevin, M., Samsing, J., Rodriguez, C., Haster, C.-J., & Ramirez-Ruiz, E. 2019, ApJ, 871, 91
Zwick, L., Capelo, P. R., Bortolas, E., Mayer, L., & Amaro-Seoane, P. 2020, MNRAS, 495, 2321
Zwick, L., Capelo, P. R., & Mayer, L. 2023, MNRAS, 521, 4645